



Three-dimensional turbulence-resolving modeling of the Venusian cloud layer and induced gravity waves. Inclusion of complete radiative transfer and wind shear

M. Lefèvre¹, S. Lebonnois¹, A. Spiga^{1,2}

¹Laboratoire de Météorologie Dynamique (LMD/IPSL), Sorbonne Université, Centre National de la Recherche Scientifique, École Polytechnique, École Normale Supérieure, Paris, France
²Institut Universitaire de France, Paris, France

Key Points:

- First 3D turbulence-resolving model of the Venus atmosphere coupled with interactive radiative scheme.
- Strong impact of the horizontal wind vertical shear on the gravity waves amplitude and wavelengths.
- 7 km convective activity resolved at cloud top due to solar absorption of the unknown UV absorber.

This article has been accepted for publication and undergone full peer review but has not been through the copyediting, typesetting, pagination and proofreading process which may lead to differences between this version and the Version of Record. Please cite this article as doi: 10.1029/2018JE005679

Corresponding author: M. Lefèvre, maxence.lefevre@lmd.jussieu.fr

Abstract

Venus' convective cloud layers and associated gravity waves strongly impact the local and global budget of heat, momentum and chemical species. Here we use for the first time three-dimensional turbulence-resolving dynamical integrations of Venus' atmosphere from the surface to 100 km altitude, coupled with fully interactive radiative transfer computations. We show that this enables to correctly reproduce the vertical position (46-55 km altitude) and thickness (9 km) of the main convective cloud layer measured by Venus Express and Akatsuki radio-occultations, as well as the intensity of convective plumes (3 m/s) measured by VeGa balloons. Both the radiative forcing in the visible and the large-scale dynamical impact play a role in the variability of the cloud convective activity with local time and latitude. Our model reproduces the diurnal cycle in cloud convection observed by Akatsuki at the low-latitudes, and the lack thereof observed by Venus Express at the equator. The observed enhancement of cloud convection at high latitudes is simulated by our model, although underestimated compared to observations. We show that the influence of the vertical shear of horizontal super-rotating winds must be accounted for in our model to allow for gravity waves of the observed intensity (>1 K) and horizontal wavelength (up to 20 km) to be generated through the "obstacle effect" mechanism. The vertical extent of our model also allows us to predict for the first time a 7-km-thick convective layer at the cloud top (70 km altitude) caused by the solar absorption of the unknown UV absorber.

1 Introduction

The strong dynamical activity inside the Venusian cloud layer has been investigated for a long time. The convective activity was measured for the first time by the Pioneer Venus radio occultation experiment [Seiff *et al.*, 1980] from 50 to 55 km above the surface and was then confirmed by other spacecraft like the Magellan probe [Hinson and Jenkins, 1995]. The variability of the vertical extension of the convective layer has been studied in detail with the VeRa radio occultation device on board of Venus Express [Tellmann *et al.*, 2009, 2012]. A strong latitudinal variability of the vertical extent of the convective layer was observed [Tellmann *et al.*, 2009], with the thickness of the convective layer reaching 10 km in polar regions, almost twice thicker than in the equatorial regions. No variability of the thickness of the convective layer with local time was measured in this dataset, though the radio occultations measured with the ongoing spacecraft Akatsuki measured a convective layer that appears to be thicker in the morning [Imamura *et al.*, 2017]. The amplitude of the vertical convective plumes, as well as the width of the convective cells, were measured in-situ by the VEGA balloons flying in the Venusian convective layer: vertical winds range between -3.5 and 2 m s⁻¹ [Linkin *et al.*, 1986] and convective cells extend horizontally from several hundred meters to tens of kilometers [Kerzhanovich *et al.*, 1986].

Gravity waves emitted by this convective layer have been observed. Radio science profiling within and above the cloud layer evidenced small-scale waves with vertical wavelengths of about 7 km [Seiff *et al.*, 1980; Counselman *et al.*, 1980]. The Venus Express instruments also measured the wavelengths of the waves emitted above the cloud layer, which range between about 2 and 3.5 km along the vertical [Tellmann *et al.*, 2012] and from 2 km to hundreds of kilometers in the horizontal [Peralta *et al.*, 2008; Piccialli *et al.*, 2014]. From the Venus Monitoring Camera (VMC) images at high latitude, the waves seem to propagate towards the pole [Piccialli *et al.*, 2014].

In addition to the convection layer inside the cloud, features observed at cloud-top by the Mariner 10 mission [Belton *et al.*, 1976] and the Pioneer Venus spacecraft [Rossow *et al.*, 1980] near subsolar point were morphologically close to convective cells with sizes between 200 and 1000 km. The VMC observed the same cellular features at the top of the cloud, approximately 70 km above the surface, at low latitude close to the subsolar point that might be attributed to convective motions [Markiewicz *et al.* [2007]; Titov *et al.*

66 [2012]. Convective cells from around 20 to a few hundreds of kilometers have been de-
67 termined from these observations. With the nine years orbiting around Venus, the Venus
68 Express mission yields a remarkable dataset of cloud top morphologies. Different regimes
69 have been determined, from mottled dark clouds at low latitude to streaky clouds around
70 50° and bright and almost featureless clouds at high latitude. Interestingly, while the low-
71 latitude cloud-top images are reminiscent of convective activity, the Venus Express and
72 Akatsuki radio occultation measurements at those altitudes in tropical regions do not show
73 any clear neutral-stability layers [Tellmann *et al.*, 2009; Ando *et al.*, 2015; Imamura *et al.*,
74 2017].

75 Aside from the observational efforts to characterize the cloud dynamics, the con-
76 vective motions in the cloud layer and the resulting emission of gravity waves have been
77 subject to modeling studies with two-dimensional models [Baker *et al.*, 1998, 2000a,b;
78 *McGouldrick and Toon*, 2008; Imamura *et al.*, 2014] and idealized three-dimensional ex-
79 periments [Yamamoto, 2014]. Recently, Lefèvre *et al.* [2017] (hereafter L17) improved on
80 those studies by proposing, for the first time, three-dimensional turbulence-resolving sim-
81 ulations with prescribed heating rates for shortwave, longwave, and large-scale dynamical
82 forcings of the convective cloud layer. This enabled to evidence the horizontal organiza-
83 tion of convective plumes as polygonal convective cells and the propagation of gravity
84 waves both above and below the convective cloud layer. L17 also concluded that the ther-
85 mal influence of the large-scale circulation (adiabatic warming/cooling associated with
86 large-scale subsiding/ascending motions) is as important as the radiative forcing of the
87 convective cloud layer. Yet, despite those improvements over existing modeling studies,
88 both the thickness of the convective layer, the intensity of the convective plumes, and the
89 amplitudes of the emitted gravity waves remained underestimated in the simulations of
90 L17 compared to the available observations.

91 The goal of this paper is to further improve on the work by L17 by carrying out
92 three-dimensional turbulence-resolving simulations with a more complete and realistic ap-
93 proach. The simulations in L17

- 94 1. did not include the wind shear present in the Venusian cloud layer where the large-
95 scale super-rotating winds increase with altitude, while the pioneering two-dimensional
96 simulations by Baker *et al.* [2000b] indicated that the wind shear had an impact
97 on the development of the convection in the cloud layer and the associated gravity
98 waves;
- 99 2. used prescribed radiative heating rates (hereafter referred to as the “offline” mode),
100 interpolated from Global Climate Modeling (GCM) calculations to the finer vertical
101 grid used for convection-resolving simulations;
- 102 3. only focused on the convective activity in the main cloud layer, with not enough
103 vertical extent to investigate a possible convective activity at the top of the main
104 cloud layer.

105 Here we propose unprecedented turbulence-resolving simulations coupled with fully
106 interactive calculations of the radiative heating rates (hereafter referred to as the “online”
107 mode) using the latest version of the radiative transfer scheme developed for the Insti-
108 tut Pierre-Simon Laplace (IPSL) Venus GCM [Lebonnois *et al.*, 2016; Garate-Lopez and
109 Lebonnois, 2018]. Furthermore, our simulations are carried out with and without the in-
110 clusion of the vertical wind shear caused by Venus’ super-rotating winds simulated in the
111 IPSL Venus GCM. With this upgraded model, we revisit the study of L17 about the con-
112 vective activity between 50 and 60 km and the induced gravity waves in the Venus cloud
113 layer, and latitudinal and temporal variability thereof. We complement this by presenting
114 the first modeling assessment of the potential convective motions at the top of the cloud at
115 an altitude of about 70 km.

116 Our paper is organized as follows. The model is described in Section 2. In Sec-
117 tion 3, the results on convective motions and gravity waves from a reference simulation
118 for the main convective region are presented, as well as the variability of this dynamical
119 activity with latitude and local time. The impact of wind shear on turbulent convection
120 in the main cloud layer is discussed in Section 4. The convective activity at the top cloud
121 layer is then investigated in Section 5. Our conclusions are summarized in Section 6.

122 2 The model

123 2.1 Dynamical core

124 Similarly to the modeling work of L17, this study is conducted using the fully-
125 compressible non-hydrostatic dynamical core of the Weather Research and Forecast (WRF)
126 terrestrial model [Skamarock and Klemp, 2008; Moeng *et al.*, 2007]. We use WRF in Large-
127 Eddy Simulations (LES) mode: the grid spacing of the WRF model is refined to a couple
128 hundreds meters so that the largest turbulent eddies (that is, convective plumes), responsi-
129 ble for most of the energy transport by buoyant convection, are resolved [Lilly, 1962; Sul-
130 livan and Patton, 2011]. Past modeling studies [Baker *et al.*, 2000a; Imamura *et al.*, 2014;
131 Lefèvre *et al.*, 2017] showed that this LES modeling strategy allows to resolve the convective
132 plumes in the unstable Venusian cloud layer, and the associated emission of gravity
133 waves. Turbulent mixing by unresolved small-scale eddies is parameterized by a subgrid-
134 scale “prognostic Turbulent Kinetic Energy” closure by Deardorff [1972], following the
135 strategy adopted for terrestrial [Moeng *et al.*, 2007] and Martian [Spiga *et al.*, 2010] LES
136 using WRF. Our Venus LES approach is not suitable to resolve small-scale turbulence in
137 stable layers of the Venus atmosphere, although it is appropriate to study the propagation
138 of gravity waves in those layers.

139 2.2 Online coupling with complete physical packages for Venus

140 The “offline” model used in L17 mainly consisted of WRF dynamical integrations
141 forced by prescribed, fixed-in-time, radiative and (large-scale) dynamical heating rates ex-
142 tracted from simulations with the IPSL Venus GCM [Lebonnois *et al.*, 2010; Lebonnois
143 *et al.*, 2016]. For the present study, we developed a complete “online” model by fully in-
144 terfacing the WRF dynamical core with the whole set of Venus LMD physical packages
145 used in the LMD Venus GCM. Our Venus LES are now designed equivalently to what
146 was done for Mars by Spiga *et al.* [2010], promoting our Venus LES from category 2 LES
147 to category 3 LES [according to the terminology described in section 2.4 of Spiga *et al.*,
148 2016].

149 The calculations of the radiative heating rates (solar and IR) are made online from
150 fluxes tables using the pressure and temperature of the domain. These calculations are per-
151 formed with a time step ratio of 1300 between the dynamical and physical timesteps, given
152 the long radiative timescales in the Venus atmosphere compared to the short timesteps
153 (about one second, see next section) used for dynamical integrations.

154 The radiative transfer used for our turbulence-resolving simulations is similar to
155 the one described in Garate-Lopez and Lebonnois [2018]. The infrared (IR) transfer is
156 based on Eymet *et al.* [2009] net-exchange rate (NER) formalism: the exchanges of en-
157 ergy between the layers are computed prior to the dynamical simulations, by separating
158 temperature-independent coefficients from the temperature-dependent Planck functions of
159 the different layers. These temperature-independent coefficients are then used in the on-
160 line model to compute the infrared cooling rates of each layer. The solar heating rates are
161 based on computations by Haus *et al.* [2015]: we use look-up tables of vertical profiles of
162 the solar heating rate as a function of solar zenith angle, that are then interpolated on the
163 fine-resolution vertical grid of our Venus LES model.

164 The cloud model is based on *Haus et al.* [2014] and *Haus et al.* [2015] and uses re-
 165 cent retrievals from Venus Express observations. This cloud model takes into account the
 166 latitudinal variation of the cloud structure, especially the cloud top variation *Haus et al.*
 167 [2014]. The latitudinal variation of the cloud is accounted for by setting 5 distinct latitude
 168 intervals: 0° to 50°, 50° to 60°, 60° to 70°, 70° to 80° and 80° to 90°. Different NER-
 169 coefficients matrices are computed for these five latitudinal bands over the 300 vertical
 170 levels of the model, ranging from the surface to roughly 100 km altitude.

171 As evidenced in L17, the heating/cooling caused by the general circulation (adia-
 172 batic cooling/heating by ascending/subsiding large-scale motions) has a significant impact
 173 on the dynamics of the convective layer. Therefore, in addition to the solar and IR radia-
 174 tive heating rates now computed online by our Venus LES, we add as in L17 a prescribed
 175 term accounting for the adiabatic cooling / warming due to the large-scale dynamics of the
 176 atmosphere. This heating rate is extracted from the IPSL Venus GCM reference simula-
 177 tion in *Garate-Lopez and Lebonnois* [2018] at the local time targeted for the Venus LES
 178 modeling. After extracting the same local time for all longitudes, a zonal mean is per-
 179 formed at the targeted latitude to remove wave-induced longitudinal perturbations. The
 180 six cases of the large-scale dynamical are shown in Figure 1 with associated large-scale
 181 vertical wind .

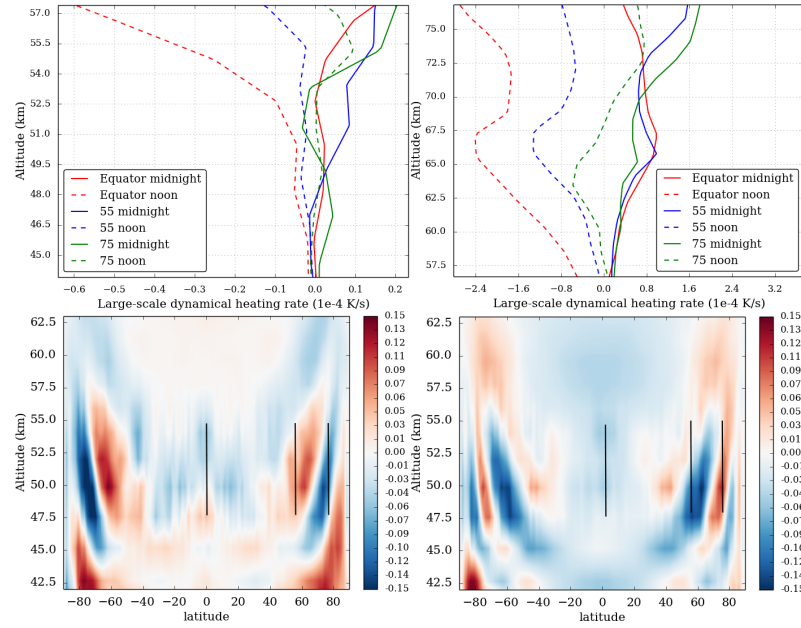
186 The dynamical equations implemented in WRF make use of potential temperature
 187 (field and perturbations) instead of temperature, while the physical packages from the
 188 IPSL Venus GCM make use of temperature. The WRF dynamical core is built with a
 189 constant heat capacity, which is set to $900 \text{ J kg}^{-1} \text{ K}^{-1}$ for this study, while the physical
 190 package uses a varying heat capacity. The conversion from potential temperature to tem-
 191 perature, and vice versa, is computed as in [*Lebonnois et al.*, 2010] using a heat capac-
 192 ity C_p varying with temperature. The initial profile of potential temperature used in the
 193 Venus LES is also computed with a varying heat capacity, to be consistent with the GCM
 194 integrations from which it is extracted.

35 2.3 Simulation settings

196 The implementation of the LMD Venus physics, and the use of the NER formal-
 197 ism for IR radiative transfer, requires the full vertical domain of the IPSL Venus GCM to
 198 operate, i.e. from the ground to ~ 100 km. The calculations are therefore carried out on
 199 this extended vertical range. The dynamical analysis in this study focuses on the Venusian
 200 cloud layer and the gravity waves emitted above this convective layer, thus all the figures
 201 presented here only display a vertical extent from 40 to 75 km. The study of the convective
 202 motions in the Planetary Boundary Layer is left for future work, as it would require
 203 different horizontal and vertical grids than the one presently adopted for the study of the
 204 cloud convection [*Yamamoto*, 2011].

207 For the sake of illustration, Figure 2 shows the three heating rates : the two solar
 208 and IR radiative rates computed by the online model and the large-scale dynamical heat-
 209 ing rate prescribed from GCM precomputed simulations and the total heating rate, at the
 210 equator at noon between 40 and 76 km. The solar heating rate is strictly positive with a
 211 maximum around 66 km due to the unknown UV absorber [*Haus et al.*, 2015]. The in-
 212 frared heating rate is mainly negative except around 46 km, the base of the cloud, where
 213 it becomes strongly positive. The dynamical heating rate is strictly negative due to the as-
 214 cending branch of the Hadley cell (Figure 1).

215 The chosen horizontal resolution for our convective cloud modeling is 400 m with a
 216 grid mesh comprising 151 points: the extent of the horizontal domain is 60x60 km. The
 217 vertical domain is composed of 300 points approximately equally distributed, except for a
 218 refined area where the convective activity takes place. The resolution inside the convective
 219 layer is in average of 150 m against 300 m for the remainder of the vertical column.



1

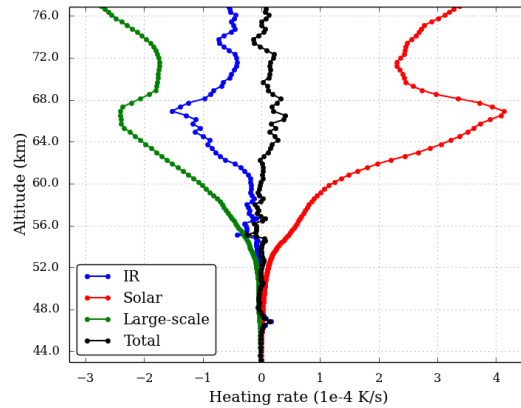
Figure 1. Top : Vertical profile of the large-scale dynamical heating rate (10^{-4} K s^{-1}) between 45 and 57 km and from 57 to 75 km. Bottom : Vertical wind of the LMD Venus GCM in (Pa s^{-1}) at night (left) and noon (right) between 42 and 63 km. Positive value of vertical means downward wind and positive value means upward wind. The black lines represent the convective activity vertical extension.

182

183

184

185



1

Figure 2. The forcing in the Venus cloud region: solar, infrared (IR), large-scale dynamical and the total heating rates (K/s) in the equatorial condition at noon.

This vertical grid is different than the one adopted in the IPSL Venus GCM, thus the NER matrices were recomputed to suit the needs of our Venus LES modeling.

The choice of spatial (horizontal and vertical) resolution requires a dynamical integration timestep of 1.5 s, as a trade-off between numerical stability and computational efficiency, and small enough to provide high temporal resolution over the lifetime of a convective cell. The horizontal boundary conditions are periodical. At the top of the domain, a Rayleigh sponge layer of 8 km height and a damping coefficient of 0.06 s^{-1} is set to avoid spurious reflection of upward-propagating gravity waves on the (artificial) model top around 100 km altitude.

229 The initial fields (temperature, pressure, winds) for the LES integrations are ex-
 230 tracted at a given latitude/local time from the IPSL Venus GCM simulation [Garate-Lopez
 231 and Lebonnois, 2018] that uses the exact same solar and IR radiative transfer as the LES
 232 integrations. In this study we performed simulations using distinct initial fields and set-
 233 tings in the physics, corresponding to several local times and latitudes. Simulations are
 234 performed using 3 different latitudes, at the equator, 55 °N and 75 °N. We choose 2 local
 235 times, midnight and noon, that are fixed during the entire corresponding Venus LES run.
 236 We remind the reader with the important point raised in L17 that *our simulations are run*
 237 *long enough so that the combination of radiative and (large-scale) dynamical heating rates*
 238 *act to destabilize the initial atmospheric profile and to cause convective instability, hence the*
 239 *mixed profile obtained in the cloud layer stems from the plumes resolved by LES integrations.*
 240 We found that running about 10 Earth days is necessary before the convective motions in
 241 our Venus LES reach a steady state at fixed local time.

242 3 Main layer : Convection and gravity waves

243 In this section, we focus on the main convective layer between 40 and 65 km. We
 244 first discuss the convective activity and gravity waves of a Venus LES run in the equato-
 245 rial conditions at noon, before analyzing the variability of this convection layer with local
 246 time and latitude. Hereafter the overline \bar{X} denotes the domain-averaged and the apostrophe
 247 X' denotes the perturbation, i.e. the fields minus the average $X' = X - \bar{X}$.

248 3.1 Simulated Convection

249 Figure 3 shows the vertical profiles of the domain-averaged potential temperature
 250 (left) and static stability (right) at the equator at noon between 42 and 65 km. The zero
 251 value of the static stability (or, equivalently, the constant value of the potential tempera-
 252 ture) indicates that the convection takes place between approximately 46.5 and 55.5 km.
 253 In the radio occultation measurements of VeRa the convective layer at the equator was
 254 located between approximately 49 and 59 km [Tellmann *et al.*, 2009]. The first radio oc-
 255 culations on-board Akatsuki [Imamura *et al.*, 2017] measured a vertical extension of the
 256 convective layer from 50 to 58 km. Thus, the bottom of the convective layer resolved in
 257 our Venus LES is slightly lower than the observations, but the thickness is consistent.

258 The predicted thickness is twice thicker in our present simulations than in the previ-
 259 ous results described in L17, which were obtained through a LES model using prescribed
 260 radiative heating rates derived from GCM calculations. We conclude that radiative trans-
 261 fer computations at fine vertical resolution is necessary to correctly reproduce the verti-
 262 cal extent of the convective layer in a turbulence-resolving model. Both above and below
 263 the convection layer stands a region of high stability, with a maximum of static stability
 264 around 63 km. Both the amplitude, and altitude of occurrence, of these stable regions are
 265 consistent with the VeRa radio occultations near the equator.

266 The convective motions are depicted in Figure 4 by two snapshots: a vertical cross
 267 section in the middle of the domain (left) and a horizontal cross section in the middle of
 268 the convective layer at 51 km (right). The values of the vertical wind vary between about
 269 2 m s⁻¹ for updrafts, and almost -3 m s⁻¹ for downdrafts. Those vertical wind veloci-
 270 ties are consistent with measurements obtained by the VeGa balloons [between -3.5 and
 271 2 m s⁻¹, Linkin *et al.*, 1986]. This is, again, a key improvement compared to our previous
 272 work in L17. As the convective layer is thicker with the complete radiative transfer, the
 273 vertical wind inside the convective layer is stronger – about twice the amplitude obtained
 274 with the prescribed heating rates.

275 The convective motions are organized on the horizontal plane as polygonal closed-
 276 cells with a “diameter” of about 20 km width. This is larger than L17, consistently so
 277 with the above-mentioned conclusions since the extent of polygonal cells scales approx-

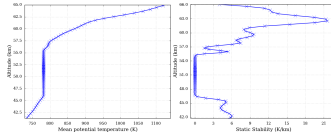


Figure 3. The Venus cloud mixing layer : domain averaged potential temperature (K) (left) and static stability (K/km) (right) between 42 and 65 km in the equatorial condition at noon.

imately with the thickness of the convective layer. These values are consistent with the broad convective cells encountered by the VeGa balloons [Kerzhanovich *et al.*, 1986]. The aspect ratio of the convective cells is quite low compared to one observed for the closed convective cells on the Earth [between 3 and 28, Atkinson and Wu Zhang, 1996].

What is the heat transport caused by the resolved convective motions in our Venus LES? Figure 5 shows the vertical convective heat flux defined as $C_p \rho \overline{w' \theta'}$ with C_p the specific heat, ρ the density calculated with the ideal gas law, w' the vertical wind perturbation and θ' the potential temperature perturbation. As is described in L17, the convective layer consists of the mixing layer, between 46.0 and 55.5 km, which is bounded by an updraft-induced entrainment layer (55.5 and 56.0 km) and a downdraft-induced entrainment layer (46.0 to 45.7 km). The convective heat flux reaches 18.0 W m^{-2} at maximum, almost twice the value obtained by the model of Imamura *et al.* [2014].

3.2 Gravity waves

Fig 6 features two snapshots of the induced gravity waves : a vertical cross section in the middle of the domain of the temperature perturbation (left) and a horizontal cross section at 57 km of the vertical wind perturbation (right). The temperature perturbations range between approximately -0.7 and 0.5 K. These values are about five times stronger than the previous version of the model described in L17, although still weaker than the VeRa observations by about a factor of two [Tellmann *et al.*, 2012]. The wave amplitude simulated by our Venus LES is consistent with the values obtained in the modeling work of Imamura *et al.* [2014] and Yamamoto [2014], with a similar vertical extent of the convective layer and no background wind. As in L17, the wavefronts in the horizontal plane are circular due to the absence of wind shear. The impact of the background wind on the gravity waves will be discussed in Section 4.

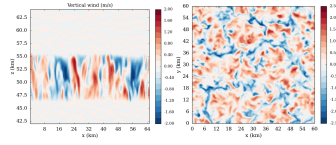


Figure 4. Snapshots of the cloud convective vertical motions : vertical cross-section at $y = 20$ km between 42 and 65 km of altitude (left) and horizontal cross-section at 51 km of the vertical wind (m s^{-1}) (right) at the Equator at noon.

Using the continuous wavelet transform¹, with the Morlet wavelet defined in *Torrence and Compo* [1998], we calculate the horizontal and vertical wavelengths of the gravity waves. Wavelet analysis indicates that the horizontal wavelengths range from 1 to 6 km at an altitude of 57 km. These values are very similar to the ones obtained with our previous model. The simulated horizontal wavelengths are on lower side of the spectrum observed by VMC [2 to 20 km, *Piccialli et al.*, 2014]. The vertical wavelength ranges from 1 to 2 km, similar to the previous model and consistent with VeRa measurements [*Tellmann et al.*, 2012].

With the formalism described in L17, and borrowed from *Frits and Alexander* [2003], the dispersion relation and group speed are calculated. A horizontal wavelength between 1 and 6 km is assumed in the two horizontal directions, with a vertical wavelength of 1.5 km, and a squared Brunt-Väisälä frequency N^2 value of 10^{-4} s^{-2} consistent with the Pioneer Venus observations [*Gierasch et al.*, 1997]. At an altitude of 57 km, this leads to an intrinsic frequency $\hat{\omega} = N^2(k^2 + l^2)/(k^2 + l^2 + m^2)$, where k , l and m the wavenumber along respectively the x-axis, the y-axis and the z-axis, between 3.3×10^{-3} and $9.0 \times 10^{-3} \text{ s}^{-1}$. The angular frequencies are close to the Brunt-Väisälä frequency, hence the gravity waves belong to high-frequency regime. Assuming zero background wind, the associated horizontal group velocity ranges from 0.18 to 2.00 m s^{-1} and the vertical component from 0.39 to 0.70 m s^{-1} .

¹ Python software by Evgeniya Predybaylo, available in this URL <http://paos.colorado.edu/research/wavelets>

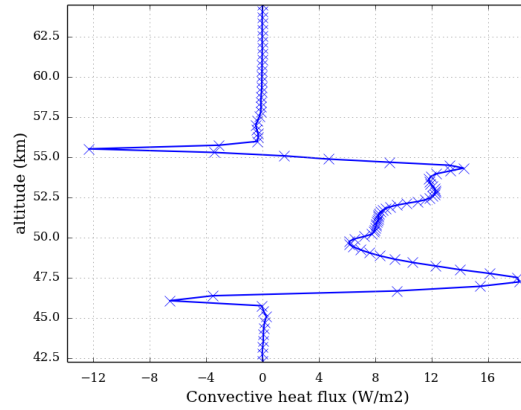


Figure 5. Domain averaged vertical profile of the turbulent heat flux (W m^{-2}) of the Venus cloud convective layer for Equatorial condition at noon.

3.3 Variability with local time and latitude

Figure 7 shows the comparison of the mean static stability at the Equator for noon and midnight between 42 and 63 km. The difference of thickness of the convective layer between noon and midnight is hardly noticeable, echoing the variability observed by the VeRa experiment. The modeling work of *Imamura et al.* [2014] found a strong solar inverse dependence on insolation, observed also in the first results of Akatsuki radio occultations. The heating at the base of the convection is driven by the IR heating in both cases. Above, at noon large-scale dynamical heating rate is negligible in front of the radiative rates whereas at night the solar heating is mainly compensated by the large-scale dynamical heating rate, resulting to a rate very close to the nighttime large-scale dynamical heating rate.

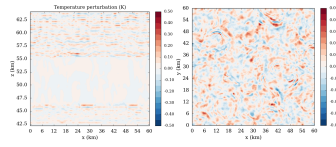


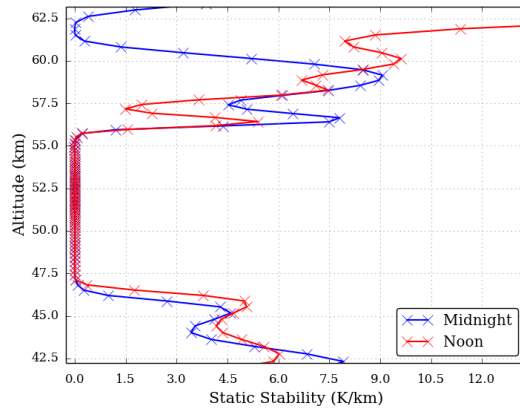
Figure 6. Snapshots of the induced gravity waves : vertical cross-section at $y = 20$ km of the temperature perturbation (K) between 42 and 65 km (left) and horizontal cross-section at 57 km of the vertical wind perturbation (m s^{-1}) (right), at the Equator at noon.

ical heating rate. At the Equator, because of the daytime large-scale dynamical heating rate, there is no variability of the convection thickness.

At midnight, a very thin 1-kilometer-deep layer of low static stability is present at approximately 62 km. The atmosphere is destabilized by the combination of IR and positive large-scale dynamical heating. The large-scale dynamical heating rate is positive and increasing constantly with altitude at night due to the large-scale descent on the nightside. The IR heating rate in that area (between 58 and 60 km) is negative and constant with altitude and decreasing above. The total rate is therefore positive around 60 km and then negative around 62 km leading to a small destabilization leading to a weak convection. At noon the strong solar heating is stabilizing this region. This unstable zone corresponds to the altitude of the decrease of the number of cloud particles in the distribution of mode 2 [Haus *et al.*, 2015]. The decrease of the number of cloud particles induces a modification of the IR heating. In our model, this destabilization is too strong compared to observations, maybe because the large-scale dynamical heating rate is not as realistic as is the radiative rate. This thin low-stability layer is also found at other latitudes and local times, approximately at the same altitude (Figures 9).

One of the key consequences of this low static stability layer lies in the perturbations of the vertical propagation of the gravity waves, similar in many aspects to the VeRa measurements [Tellmann *et al.*, 2012]. Figure 8 shows a comparison of the temperature perturbations (K) at the Equator for noon (left) and midnight (right) between 42 and 63 km. The amplitude of the waves is slightly stronger at midnight, due to the stronger convection, but what is mostly noticeable is the strong attenuation around 61 km induced by the low static stability layer.

Radio-occultation profiling of the convective layer [Tellmann *et al.*, 2009; Ando *et al.*, 2015; Imamura *et al.*, 2017] shows that the thickness of the convective layer increases with



1

Figure 7. Comparison of the vertical profile of the domain averaged static stability (K/km) for equatorial condition at noon and midnight between 42 and 63 km.

latitude. Both the bottom and top boundaries of the convective layer also appear to change with latitude. No variability with local time was observed with the Venus Express measurements whereas some amount of variability was detected by Akatsuki. Figure 9 shows the comparison of the mean static stability for the three latitudes at noon (left) and midnight (right). To be able to compare properly the latitudinal cases, the 2 figures are presented with pressure as y-axis. At noon the convective thickness for the Equator and 55° latitude are very close, whereas at 75° the convective layer extends towards a higher altitude – almost 2 km higher. At midnight the convective thickness for the Equator and 75° are very similar while at 55° latitude the convective layer goes at higher altitude, about 3 km higher.

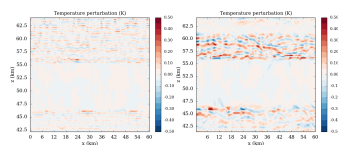


Figure 8. Comparison of the induced gravity waves : temperature perturbation (K) at the Equator for noon (left) and midnight (right) between 42 and 63 km.

The altitude of the bottom boundary of the convective layer does not change with latitude nor with local time. The bottom of the convective layer is controlled by the maximum of IR heating, that does not change in altitude because the cloud bottom is fixed in the cloud model *Haus et al.* [2015], although variations of the bottom cloud boundary are observed [*Cimino, 1982; Barstow et al., 2012*]. Meanwhile the top boundary of the convective layer does vary with latitude and local time. The top of the convective layer is controlled by the energy exchange between the cloud and space through a maximum of IR cooling. At 55° latitude at midnight, the large-scale dynamical heating rate is positive due to the descending branch of the Hadley cell (Figure 1) and superior in amplitude to the IR radiative rate. The total rate is positive almost along the entire convective layer, adding more heat to be mixed. Therefore the convection needs to go at higher altitude. At noon, the large-scale dynamical heating rate is negative and compensates the solar heating inside the convective layer. At 75° a similar mechanism is at play. At noon, the large-scale dynamical heating rate is positive along the convective layer, adding with the solar heating more heat to be mixed, while at midnight the large-scale dynamical heating rate is negligible compared to the IR cooling. Both the top and bottom boundaries of the convective layer are controlled by the IR radiative transfer, but the large-scale dynamical heating rate can play a key role to modify the top of the layer.

Another factor that is variable with latitude is the time for the convection to develop and reach a steady state. With the implementation of the radiative scheme, this time increased: in the “offline” simulations of L17 it was 1 to 2 Earth days, while in the present “online” simulations it is from 4 to more than 10 Earth days. The implementation of the latitudinal variability of the cloud induced a modification of the large-scale dynamical heating rates in the convective region. The development of the convection to stabilize this region is affected by these different large-scale dynamical heating rates. A second possible explanation for the longer time needed to reach steady-state is that including the full radiative transfer scheme couples the temperature structure and the IR cooling rates. When

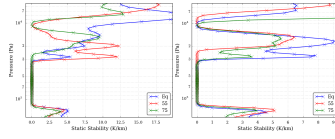


Figure 9. Comparison of the vertical profile of the domain averaged static stability (K/km) for the Equator, 55° and 75° of latitude at noon (left) and midnight (right).

developing, the convective layer appears first separated in two convective layers that end up connecting each other and forming one single convective layer, as shown in Figure 4. This two-convective-layer transient phase remains for a longer time at 55°. Such a separation in the convective layer appeared in some of the observed Magellan static stability profiles [Hinson and Jenkins, 1995]. Our simulations suggest that this may be related to the influence of the large-scale dynamical heating rate.

The “online” coupling of the turbulence-resolving WRF dynamical core with the LMD physics radiative scheme enables our Venus LES runs to reproduce a convective layer that is more in agreement with the observations, especially at high latitudes, than the “offline” Venus LES presented in L17 with prescribed heating rates. A vertically-refined radiative transfer was crucial to model properly the Venus cloud convective layer. The variations with latitude and local time of the convective layer are also more consistent with observations in our “online” Venus LES than in the “offline” version presented in L17. Despite the better agreement with observations for the convective layer, the induced gravity waves amplitude and wavelengths remain below measured values. We now turn to Venus LES including wind shear to address this remaining discrepancy.

4 Impact of the wind shear

In this section we will study the impact of the wind shear on the convection and induced gravity waves. We carried out Venus LES runs similar to the ones described in the previous section, except that an ambient (background) wind profile is prescribed throughout the simulations. Figure 10 shows this background zonal and meridional wind at noon (left) and midnight (right) vertical profile. Those profiles of background winds are the same in every grid points of the LES domain. They are extracted from the IPSL Venus GCM simulation of *Garate-Lopez and Lebonnois* [2018] and interpolated on the LES vertical grid. Please note that positive meridional velocity means poleward velocity.

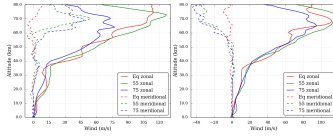
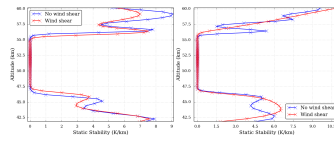


Figure 10. Vertical profile of the input zonal and meridional winds at noon (left) and midnight (right) for the Equator, 55° and 75° of latitude.

The comparison of the mean static stability profile with or without wind shear at the Equator at midnight (left) and noon (right) is shown in Figure 11. The impact of the presence of the wind shear on the vertical extent of the convective layer is hardly noticeable. This conclusion stands for higher-latitude Venus LES runs. This is expected since the convection of the Venusian cloud layer is mostly buoyancy-driven and not shear-driven.

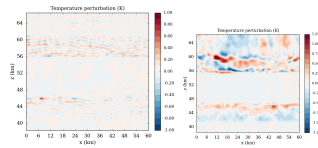
The impact of wind shear is expected to be significant on the gravity waves emitted by convective motions in the cloud. Wind shear modifies the frequency of the wave $\omega = \hat{\omega} + \vec{k} \cdot \vec{U}$ (with $\hat{\omega}$ the intrinsic frequency, \vec{k} the wave vector and \vec{U} the horizontal wind vector), thus the horizontal phase and group wave speed. It also has an impact on the gravity wave source. In addition to the generation of waves by the updrafts and downdrafts, similar to a mechanical oscillator [Clark *et al.*, 1986; Ansong and Sutherland, 2010], the interaction of the flow with the convective overshoot also causes a secondary wave generation to occur, called the obstacle effect [Mason and Sykes, 1982; Clark *et al.*, 1986]. The overshoot both below and above the convective layer are acting like low hills in orographically-triggered gravity waves near the surface. The generation of gravity waves by the mechanical oscillator effect is characterized by high frequencies and short wavelengths with preferred horizontal direction propagation, while the obstacle effect produces longer wavelength features propagating against the background wind [Fovell *et al.*, 1992]. The first modeling studies with three-dimensional simulations of convection and convectively generated gravity waves from the surface to 100 km has been performed by Horinouchi *et al.* [2002]; Horinouchi [2004]. On Venus, numerical modeling by Baker *et al.* [2000b] evidenced that the impact of the wind shear was strong on the generation and propagation of gravity waves. Yamamoto [2014] found a similar trend on the gravity waves by increasing the background wind.

Figures 12 and 13 show the comparison of two snapshots of the temperature (K) and vertical wind (m s^{-1}) perturbations at the Equator at midnight without (left) and with (right) wind shear. In the case of the presence of the wind shear, the amplitude of the



441
442
443

Figure 11. Comparison of the vertical profile of the domain averaged static stability (K/km) at cloud top between the presence of a wind shear and no wind shear for equatorial condition at midnight (left) and noon (right).



63
64

Figure 12. Impact of the wind shear : Comparison of two snapshots of the temperature perturbation (K) at the Equator at midnight without (left) and with (right) wind shear.

468

waves is more than twice larger than that in the no wind shear case, reaching values of

about ± 1.5 K, the same order of magnitude that the waves observed [Tellmann *et al.*, 2012]. Above the convective layer, most of the waves propagate toward the west, significant of the obstacle effect wave, but there is also some waves propagating toward the east. In Earth studies, the vast majority of the waves generated by the obstacle propagate against the background wind [Fovell *et al.*, 1992]. For Venus, one possibility is that the ratio between the waves produced by the obstacle effect mechanism against the mechanical oscillator is closer to the equilibrium than the Earth, additional study is needed to understand this effect. The morphology of the wavefronts is also deeply impacted: wavefronts are linear in the wind-shear case in contrast to the circular wavefronts found in the no-wind shear case. Using the same methodology as in Section 3, we estimate that at 57 km, the gravity waves have a typical horizontal wavelength of 10 km. In presence of the wind shear, the vertical wavelength reaches more than 4 km, very close to VeRa measurements [Tellmann *et al.*, 2012]. The intrinsic frequency $\hat{\omega}$ of the gravity waves at 57 km is of $5 \times 10^{-3} \text{ s}^{-1}$. At 57 km, the mean horizontal flow is about 67 m s^{-1} and the waves are advected with the flow, therefore the frequency ω is $3.6 \times 10^{-2} \text{ s}^{-1}$. The corresponding group velocity is between 2.8 m s^{-1} on the vertical and 74 m s^{-1} on the horizontal. The direction of the wavefront is east-west, as is expected by the filtering exerted by the meridional component of the wind.

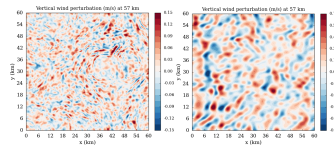
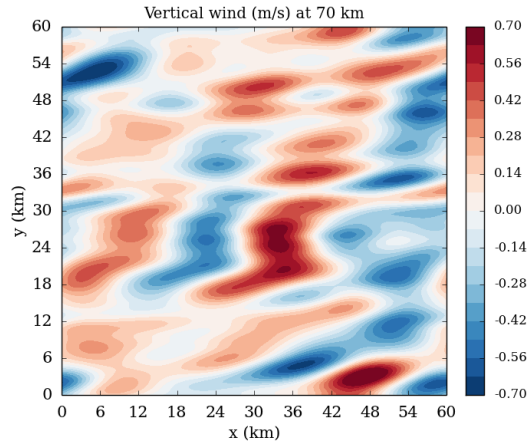


Figure 13. Comparison of two snapshots of the vertical wind perturbation (m s^{-1}) at the Equator at midnight without (left) and with (right) wind shear.

The wind shear also has a strong impact at higher altitude. Figure 14 shows a snapshot of the vertical wind perturbation (m s^{-1}) at 70 km at the Equator at midnight in presence of wind shear. At this altitude, the gravity waves have a similar amplitude that as 57 km with also a linear wavefront but with greater wavelengths. The typical horizontal wavelength is of 20 km, on the higher part of spectra of wavelength measured by VMC [Piccialli *et al.*, 2014]. The wave intrinsic frequency $\hat{\omega}$ ranges from $1.9 \times 10^{-3} \text{ s}^{-1}$. At 70 km, the mean horizontal wind velocity is approximately 106 m s^{-1} . Therefore the frequency ω is $3.1 \times 10^{-2} \text{ s}^{-1}$. The associated group velocity is on the vertical 1.2 m s^{-1} and on the horizontal 112 m s^{-1} . The waves are advected with the flow, at 57 km the

498 zonal is much stronger than the meridional wind (see Figure 10) therefore the direction
 499 of the phase propagation is east-west. At cloud top at high latitude, the zonal wind and
 500 meridional wind are close in amplitude, resulting to an horizontal wind more directed to
 501 the poles than at the Equator and thus a phase speed of the gravity wave more oriented
 502 towards the poles. This tendency of gravity waves to propagate towards the pole at mid-
 503 to-high latitudes is clearly observed in VMC observations [Piccialli *et al.*, 2014].



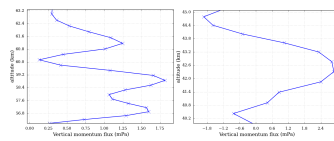
1

504 **Figure 14.** Snapshots of the vertical wind perturbation (m s^{-1}) at 70 km at the Equator at midnight in
 505 presence of wind shear.

506 To assess the impact of the gravity waves on the large-scale dynamical heating rate
 507 when they break, we evaluate the momentum transport with the Eliassen-Palm flux us-
 508 ing the formalism of *Andrews* [1987] and *Lott et al.* [2012], we focus here on the verti-
 509 cal component of the flux $-\overline{\rho u'w'}$. Figure 15 shows the vertical angular momentum flux
 510 above and below the convective layer at the equator. The flux is strictly positive above

511 the convective layer, while alternating between positive and negative values below. The
 512 vertical angular momentum flux reaches values of almost 3 mPa. At the altitude of the
 513 convective layer the density of the atmosphere of Venus is comparable to the density of
 514 the surface on Earth therefore we can compare the vertical momentum flux from gravity
 515 waves on the two planets. For Earth, convectively generated gravity waves momentum flux
 516 has been estimated with cloud-resolving model by [Horinouchi *et al.*, 2002] at approxima-
 517 tively 0.2 mPa, an order of magnitude smaller.

518 The implementation of wind shear leads to the generation by the convection of more
 519 realistic gravity waves, compared to available observations. The calculation of the vertical
 520 angular momentum flux of these waves may be used to improve the GCM parameteriza-
 521 tion of the subgrid gravity waves based on *Lott and Guez* [2013] and recently used in the
 522 IPSL Venus GCM [*Gilli et al.*, 2017].



524 **Figure 15.** Domain averaged vertical momentum flux (mPa) above (left) and below (right) the convective layer at the equator.

5 Dynamics at the top of the cloud

Convective features near the equator at subsolar point have been observed by Pioneer Venus through the unknown UV-absorber [Rossow *et al.*, 1980; Schubert *et al.*, 1980], suggesting cellular structure of 10^3 km width. Using as well the unknown UV-absorber, VMC/Venus Express observed convective structures at low latitude at the subsolar point, which were interpreted as cellular features of a diameter between tens of kilometers and few hundreds of kilometers [Markiewicz *et al.*, 2007; Titov *et al.*, 2012].

The figures shown below are without wind shear. Figure 16 shows the mean potential temperature and static stability between 63 and 75 km in our Venus LES run in equatorial conditions at noon. The presence of a zero-static-stability layer indicates that the convection takes place between approximately 66.5 and 73.0 km. This is in line with the convective features observed in the UV by Pioneer Venus and Venus Express. However, no mixed layer has been detected in radio-occultations at this altitude, neither by Magellan [Hinson and Jenkins, 1995], Venus Express [Tellmann *et al.*, 2009] nor Akatsuki [Imamura *et al.*, 2017]. At this altitude, the atmosphere profiled by radio-occultations is very stable (the static stability is several Kelvin per kilometer).

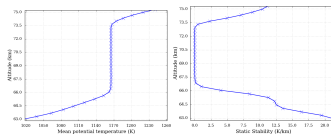


Figure 16. Domain averaged vertical profile of potential temperature (K) (left) and static stability (K/km) (right) between 63 and 75 km at the equator at noon.

The convective motions that underlie the mixing layer in Figure 16 are shown in Figure 17, with two snapshots of: a vertical cross section in the middle of the domain and a horizontal cross section in the middle of the convective layer at 70 km. The vertical wind ranges between 2.7 and -3.5 m s^{-1} . The convection is organized, similarly to the main cloud layer, as polygonal closed cells of diameter about 15 to 20 km, consistent with the smallest cells observed in the Venus Express images [Markiewicz *et al.*, 2007].

To understand the source behind this convective activity, we need to look at the heating rates (Fig 18). The bottom of the convective layer is located at the maximum of solar heating (66 km) creating a maximum positive value of the total heating rate. The top

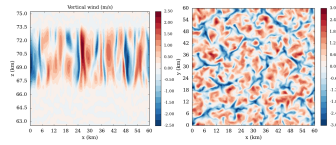


Figure 17. Snapshots of the convective vertical motions: vertical cross-section at $y=20$ km between 63 and 75 km (left) and horizontal cross-section at 51 km of the vertical wind (m s^{-1}) (right) for equatorial condition at noon.

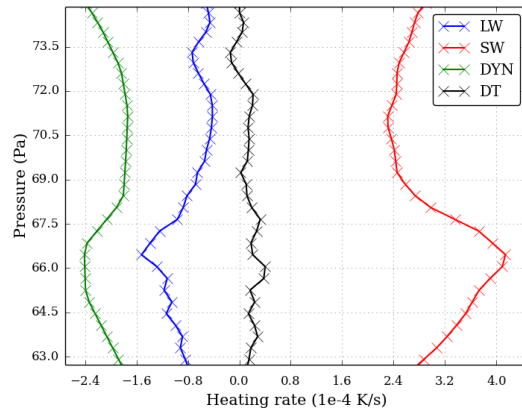
of the convection is located where the local maximum cooling of the IR heating rate (approximately 73 km), as well as the large-scale dynamical heating rate, are creating a minimum negative value of the total heating rate. The heating resulting from the absorption of the solar flux by the unknown UV absorber destabilizes the atmosphere and initiates convective activity.

Figure 19 shows the vertical profile of the turbulent heat flux defined above. The behavior is similar to the convective layer below, with a mixing layer (66.5 to 73.3 km) capped between an entrainment layer dominated downdraft-induced ones (65.6 to 66.5 km) and an entrainment layer dominated by the updraft-induced ones (73.3 to 74.0 km). Despite stronger vertical wind the cloud top convective heat flux is weaker than the convection below, because of the decrease with altitude of the density and heat capacity.

The gravity waves emitted by the cloud top convective activity are very similar to the ones emitted from the convective layer below. The amplitude of the waves is less than a Kelvin and the vertical wavelength is from 1 to 2 km and from 1 to 5 km for the horizontal wavelength.

In Venus Express imaging observations, the convective activity at cloud top is present at low latitude close to the subsolar point. We can investigate this variability with local time and latitude with our Venus LES results. The comparison of the mean static stability in the 63–75 km at the Equator between midnight and noon is shown in Figure 20. The difference is clear between the two local times: at midnight the atmosphere is stable, with the exception of a layer of small static stability of few hundred meters where no convective plumes develop. The absence of heating by the sun inhibits the cloud top convection.

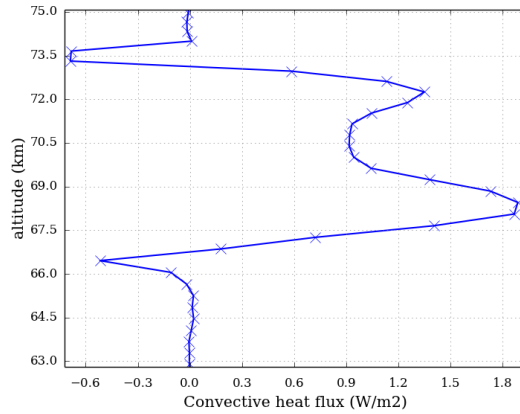
Figure 21 shows the comparison of the mean static stability at noon between the equator : 55° and 75° of latitude between 63 and 75 km. There is a clear variability with



1

560 **Figure 18.** Venus cloud top forcing : solar (SW), infrared (LW), dynamical (DYN) and total (DT) heating
 561 rates (K/s) between 63 and 75 km at the equator at noon.

585 latitude, the cloud-top convective layer present at the Equator is also present at 55° lati-
 586 tude, while not present at all at 75°. The total heating rate at 75° between 66 and 75 km
 587 has no clear-cut behavior and oscillates around zero, and therefore does not induce strong
 588 destabilization. This behavior is caused by the weaker solar heating and the large-scale dy-
 589 namical heating rate, that is positive and negative in that region. At 55° latitude, although
 590 weaker than at the Equator, the solar heating is still able to destabilize the atmosphere and
 591 enhance convection. However, the dynamics of the atmosphere is dominated at these alti-
 592 tudes by the equatorial jet and mid-latitude jets between 40 and 50° latitude [*Sánchez-*
 593 *Lavega et al., 2017*]. In the IPSL Venus GCM, the jets are reproduced [*Garate-Lopez and*
 594 *Lebonnois, 2018*] but the mid-latitude jet is located between 50 and 60°, poleward to the
 595 observed jet. Therefore, the large-scale dynamical heating rate at 55° latitude may not be
 596 representative of the observed Venus environment at 55° latitude while the IR and solar

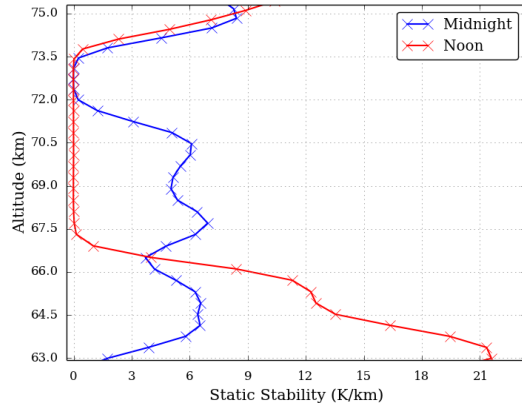


1

Figure 19. Domain averaged vertical profile of the turbulent heat flux (W m^{-2}) of the Venus cloud top convection between 63 and 75 km for equatorial condition at noon.

rates are realistic, so the comparison between the modeled and observed 55° latitude cloud convective activity is difficult. Beyond the jets, at 65° the large-scale dynamical heating rate (not shown here) at these altitudes has similar behavior as the 75° case and does not induce cloud top convective activity.

To the extent of our knowledge, this is the first modeling of top-of-the-cloud convective activity. At noon the solar heating from the unknown UV absorber destabilizes the atmosphere and enhances convection. Observations of the cloud top at noon show convective activity only at low latitude while around 50° , the clouds are streaky, suggesting a laminar flow. In our model, we have convective activity at cloud top at both the Equator and 55° latitude. The large-scale dynamical heating rate plays a role in inhibiting the convective activity. The unknown absorber being the source of this convective activity, the



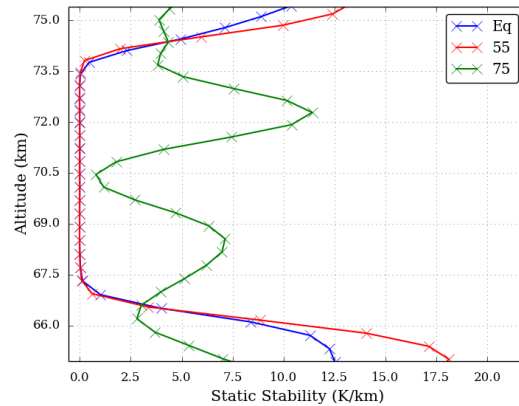
1

581 **Figure 20.** Comparison of the domain averaged static stability vertical profile (K/km) for equatorial
 582 conditions at noon and at midnight between 63 and 75 km.

610 uncertainty about its abundance and optical properties used for the calculation of the solar
 611 heating rate [Haus *et al.*, 2015] may affect the characteristics of the cloud top convective
 612 activity. Furthermore, the conundrum between, on the one hand, LES and imagery that
 613 hints at convective motions, and on the other hand, radio-occultations that indicate a very
 614 stable atmosphere, will have to be solved in future observational and modeling studies.

615 **6 Conclusion**

616 With the coupling of the WRF LES mode to the Venus LMD physics, we simulate
 617 a main convective layer that has characteristics close to the observations. Both the thick-
 618 ness of the main convective layer and the cell diameter, as well as the convective vertical



1

Figure 21. Comparison of the domain averaged static stability vertical profile (K/km) at noon (LT 12 h), for the Equator, 55° latitude and 75° latitude between 63 and 75 km.

winds, are consistent with measurements from past and ongoing missions. Using the LMD radiative scheme with a fine vertical resolution is needed to reproduce a realistic convective layer. However, some discrepancies remain with observations. The variability with local time is hardly noticeable contrary to the first Akatsuki measurements. The variability with latitude is consistent with the VeRa observations for the Equator and 75° but the 55° latitude case is too close to the Equator case. As in the previous study, the large-scale dynamical heating is interpolated from the 50 GCM vertical levels to the 300 LES levels. Higher vertical resolution GCM runs could improve the large-scale dynamical heating rate. Changes in the dynamical core of the GCM should improve the angular momentum conservation and polar region modeling, and therefore the general circulation and the large-scale dynamical heating rate.

To improve the realistic aspect of the model, wind shear was taken into account. The effect on the convective layer is hardly noticeable whereas it is strong on the gravity waves. In addition to mechanical oscillator mechanism, the obstacle effect wave mechanism is now present. This additional wave production mechanism has the effect to generate gravity waves with higher amplitude. The horizontal wavelengths are also higher and closer to the observations. This process has to be taken into account to model properly the gravity waves associated with the convective activity.

The vertical extension of the model made it possible to study the cloud-top cell features observed at low latitude at the subsolar point. The solar heating from the unknown UV absorber destabilizes the atmosphere and our model predicts convective activity of about 6 km in the vertical that could be at the origin of these observed cell features. However, none of the radio occultation experiments observed a mixed layer at the altitude; a very stable atmosphere is observed. Convective activity at 55° latitude is also obtained in our simulations, though only streaky clouds are observed at these latitudes. Possible explanations for this discrepancy include the distribution of the unknown UV absorber as well as discrepancy in the large-scale dynamical heating rate, that is not fully representative of the actual 55° latitude environment in the IPSL Venus GCM simulations.

Our model is now able to reproduce realistic cloud convective activity and associated gravity waves, and is a tool to interpret the observations of the subsolar convective activity. Coupled with the photochemistry and microphysical schemes of the IPSL Venus GCM, the present model could investigate the impact of the mesoscale dynamics on the cloud formation and variability.

Acknowledgments

The authors acknowledge financial support from Centre National d'Études Spatiales (CNES) and Programme National de Planétologie (PNP). Simulations were performed at CINES, France, under the project n°1116 and at Sorbonne Université with HPCaVe. We would like to thank Dr. Takeshi Horinouchi and the second anonymous reviewer for their reviews that help improve the paper. Simulation results used to obtain the figures in this paper are available in the open online repository <https://figshare.com/s/03a0497e6537dbbca4ba>. Full simulation results performed in this paper are available upon reasonable request (contact: maxence.lefevre@lmd.jussieu.fr).

References

- Ando, H., T. Imamura, T. Tsuda, S. Tellmann, M. Pätzold, and B. Häusler (2015), Vertical Wavenumber Spectra of Gravity Waves in the Venus Atmosphere Obtained from Venus Express Radio Occultation Data: Evidence for Saturation, *Journal of Atmospheric Sciences*, *72*, 2318–2329, doi:10.1175/JAS-D-14-0315.1.
- Andrews, D. G. (1987), On the interpretation of the Eliassen-palm flux divergence, *Quarterly Journal of the Royal Meteorological Society*, *113*, 323–338, doi:10.1002/qj.49711347518.
- Ansong, J. K., and B. R. Sutherland (2010), Internal gravity waves generated by convective plumes, *Journal of Fluid Mechanics*, *648*, 405, doi:10.1017/S0022112009993193.
- Atkinson, B. W., and J. Wu Zhang (1996), Mesoscale shallow convection in the atmosphere, *Reviews of Geophysics*, *34*, 403–431, doi:10.1029/96RG02623.
- Baker, R. D., G. Schubert, and P. W. Jones (1998), Cloud-Level Penetrative Compressible Convection in the Venus Atmosphere., *J. of Atm. Sc.*, *55*, 3–18, doi:10.1175/1520-0469(1998)055<0003:CLPCCI>2.0.CO;2.
- Baker, R. D., G. Schubert, and P. W. Jones (2000a), Convectively generated internal gravity waves in the lower atmosphere of Venus. I. No wind shear., *J. of Atm. Sc.*, *57*, 184–199, doi:10.1175/1520-0469(2000)057<0184:CGIGWI>2.0.CO;2.

- 679 Baker, R. D., G. Schubert, and P. W. Jones (2000b), Convectively generated internal
680 gravity waves in the lower atmosphere of Venus. II. Mean wind shear and wave-mean
681 flow interaction., *J. of Atm. Sc.*, *57*, 200–215, doi:10.1175/1520-0469(2000)057<0200:
682 CGIGWI>2.0.CO;2.
- 683 Barstow, J. K., C. C. C. Tsang, C. F. Wilson, P. G. J. Irwin, F. W. Taylor, K. Mc-
684 Gouldrick, P. Drossart, G. Piccioni, and S. Tellmann (2012), Models of the global cloud
685 structure on Venus derived from Venus Express observations, *Icarus*, *217*, 542–560,
686 doi:10.1016/j.icarus.2011.05.018.
- 687 Belton, M. J. S., G. R. Smith, G. Schubert, and A. D. del Genio (1976), Cloud patterns,
688 waves and convection in the Venus atmosphere, *Journal of Atmospheric Sciences*, *33*,
689 1394–1417, doi:10.1175/1520-0469(1976)033<1394:CPWACI>2.0.CO;2.
- 690 Cimino, J. (1982), The composition and vertical structure of the lower cloud deck on
691 Venus, *Icarus*, *51*, 334–357, doi:10.1016/0019-1035(82)90088-4.
- 692 Clark, T. L., T. Hauf, and J. P. Kuettner (1986), Convectively forced internal gravity
693 waves: Results from two-dimensional numerical experiments, *Quarterly Journal of the*
694 *Royal Meteorological Society*, *112*, 899–925, doi:10.1002/qj.49711247402.
- 695 Counselman, C. C., S. A. Gourevitch, R. W. King, G. B. Lorient, and E. S. Ginsberg
696 (1980), Zonal and meridional circulation of the lower atmosphere of Venus deter-
697 mined by radio interferometry, *Journal of Geophysical Research*, *85*, 8026–8030, doi:
698 10.1029/JA085iA13p08026.
- 699 Deardorff, J. W. (1972), Numerical Investigation of Neutral and Unstable Plane-
700 tary Boundary Layers., *Journal of Atmospheric Sciences*, *29*, 91–115, doi:10.1175/
701 1520-0469(1972)029<0091:NIONAU>2.0.CO;2.
- 702 Eymet, V., R. Fournier, J.-L. Dufresne, S. Lebonnois, F. Hourdin, and M. A. Bullock
703 (2009), Net exchange parameterization of thermal infrared radiative transfer in Venus'
704 atmosphere, *J. of Geophys. Res. (Planets)*, *114*, E11008, doi:10.1029/2008JE003276.
- 705 Fovell, R., D. Durran, and J. R. Holton (1992), Numerical Simulations of Convectively
706 Generated Stratospheric Gravity Waves., *Journal of Atmospheric Sciences*, *49*, 1427–
707 1442, doi:10.1175/1520-0469(1992)049<1427:NSOCGS>2.0.CO;2.
- 708 Frits, D. C., and M. J. Alexander (2003), Gravity wave dynamics and effects in the middle
709 atmosphere, *Rev. of Geoph.*, *41*, 1112–1131, doi:10.1029/2001RG000106.
- 710 Garate-Lopez, I., and S. Lebonnois (2018), Latitudinal Variation of Clouds' Structure Re-
711 sponsible for Venus' Cold Collar, *Icarus*.
- 712 Gierasch, P. J., R. M. Goody, R. E. Young, D. Crisp, C. Edwards, R. Kahn, D. Rider,
713 A. del Genio, R. Greeley, A. Hou, C. B. Leovy, D. McCleese, and M. Newman (1997),
714 The General Circulation of the Venus Atmosphere: an Assessment, in *Venus II: Geol-
715 ogy, Geophysics, Atmosphere, and Solar Wind Environment*, p. 459.
- 716 Gilli, G., S. Lebonnois, F. González-Galindo, M. A. López-Valverde, A. Stolzenbach,
717 F. Lefèvre, J. Y. Chaufray, and F. Lott (2017), Thermal structure of the upper atmo-
718 sphere of Venus simulated by a ground-to-thermosphere GCM, *Icarus*, *281*, 55–72, doi:
719 10.1016/j.icarus.2016.09.016.
- 720 Haus, R., D. Kappel, and G. Arnold (2014), Atmospheric thermal structure and cloud fea-
721 tures in the southern hemisphere of Venus as retrieved from VIRTIS/VEX radiation
722 measurements, *Icarus*, *232*, 232–248, doi:10.1016/j.Icarus.2014.01.020.
- 723 Haus, R., D. Kappel, and G. Arnold (2015), Radiative heating and cooling in the middle
724 and lower atmosphere of Venus and responses to atmospheric and spectroscopic param-
725 eter variations, *Planetary and Space Science*, *117*, 262–294, doi:10.1016/j.pss.2015.06.
726 024.
- 727 Hinson, D. P., and J. M. Jenkins (1995), Magellan radio occultation measurements of at-
728 mospheric waves on Venus, *Icarus*, *114*, 310–327, doi:10.1006/icar.1995.1064.
- 729 Horinouchi, T. (2004), Simulated breaking of convectively generated mesoscale gravity
730 waves and airglow modulation, *Journal of Atmospheric and Solar-Terrestrial Physics*, *66*,
731 755–767, doi:10.1016/j.jastp.2004.01.023.
- 732 Horinouchi, T., T. Nakamura, and J.-i. Kosaka (2002), Convectively generated mesoscale

- 733 gravity waves simulated throughout the middle atmosphere, *Geophysical Research Let-*
 734 *ters*, 29, 2007, doi:10.1029/2002GL016069.
- 735 Imamura, T., T. Higuchi, Y. Maejima, M. Takagi, N. Sugimoto, K. Ikeda, and H. Ando
 736 (2014), Inverse insolation dependence of Venus' cloud-level convection, *Icarus*, 228,
 737 181–188, doi:10.1016/j.Icarus.2013.10.012.
- 738 Imamura, T., H. Ando, S. Tellmann, M. Pätzold, B. Häusler, A. Yamazaki, T. M. Sato,
 739 K. Noguchi, Y. Futaana, J. Oschlisniok, S. Limaye, R. K. Choudhary, Y. Murata,
 740 H. Takeuchi, C. Hirose, T. Ichikawa, T. Toda, A. Tomiki, T. Abe, Z.-i. Yamamoto,
 741 H. Noda, T. Iwata, S.-y. Murakami, T. Satoh, T. Fukuhara, K. Ogohara, K.-i. Sugiyama,
 742 H. Kashimura, S. Ohtsuki, S. Takagi, Y. Yamamoto, N. Hirata, G. L. Hashimoto,
 743 M. Yamada, M. Suzuki, N. Ishii, T. Hayashiyama, Y. J. Lee, and M. Nakamura (2017),
 744 Initial performance of the radio occultation experiment in the Venus orbiter mission
 745 Akatsuki, *Earth, Planets, and Space*, 69, 137, doi:10.1186/s40623-017-0722-3.
- 746 Kerzhanovich, V. V., Y. N. Aleksandrov, R. A. Andreev, N. A. Armand, R. V. Bakitko,
 747 J. E. Blamont, L. Boloh, C. E. Hildebrand, S. P. Ignatov, A. P. Ingersoll, V. P. Lysov,
 748 B. I. Mottuslev, G. Petit, K. M. Pichkhadze, R. A. Preston, V. A. Vorontsov, A. S.
 749 Vyshlov, R. E. Young, and A. L. Zaitsev (1986), Smallscale Turbulence in the Venus
 750 Middle Cloud Layer, *Soviet Astronomy Letters*, 12, 20–22.
- 751 Lebonnois, S., F. Hourdin, V. Eymet, A. Cresspin, R. Fournier, and F. Forget (2010), Su-
 752 perrotation of Venus' atmosphere analyzed with a full general circulation model, *J. of*
 753 *Geophys. Res. (Planets)*, 115, E06006, doi:10.1029/2009JE003458.
- 754 Lebonnois, S., N. Sugimoto, and G. Gilli (2016), Wave analysis in the atmosphere of
 755 Venus below 100-km altitude, simulated by the LMD Venus GCM, *Icarus*, 278, 38 –
 756 51, doi:10.1016/j.icarus.2016.06.004.
- 757 Lefèvre, M., A. Spiga, and S. Lebonnois (2017), Three-dimensional turbulence-resolving
 758 modeling of the Venusian cloud layer and induced gravity waves, *Journal of Geophysi-*
 759 *cal Research (Planets)*, 122, 134–149, doi:10.1002/2016JE005146.
- 760 Lilly, D. K. (1962), On the numerical simulation of buoyant convection, *Tellus*, 14(2),
 761 148–172.
- 762 Linkin, V. M., V. V. Kerzhanovich, A. N. Lipatov, K. M. Pichkadze, A. A. Shurupov,
 763 A. V. Terterashvili, A. P. Ingersoll, D. Crisp, A. W. Grossman, R. E. Young, A. Seiff,
 764 B. Ragent, J. E. Blamont, L. S. Elson, and R. A. Preston (1986), VEGA balloon dy-
 765 namics and vertical winds in the Venus middle cloud region, *Science*, 231, 1417–1419,
 766 doi:10.1126/science.231.4744.1417.
- 767 Lott, F., and L. Guez (2013), A stochastic parameterization of the gravity waves due to
 768 convection and its impact on the equatorial stratosphere, *Journal of Geophysical Re-*
 769 *search (Atmospheres)*, 118, 8897–8909, doi:10.1002/jgrd.50705.
- 770 Lott, F., L. Guez, and P. Maury (2012), A stochastic parameterization of non-orographic
 771 gravity waves: Formalism and impact on the equatorial stratosphere, *Geophysical Re-*
 772 *search Letters*, 39, L06807, doi:10.1029/2012GL051001.
- 773 Markiewicz, W. J., D. V. Titov, S. S. Limaye, H. U. Keller, N. Ignatiev, R. Jaumann,
 774 N. Thomas, H. Michalik, R. Moissl, and P. Russo (2007), Morphology and dynamics
 775 of the upper cloud layer of Venus, *Nature*, 450, 633–636, doi:10.1038/nature06320.
- 776 Mason, P. J., and R. I. Sykes (1982), A two-dimensional numerical study of horizontal roll
 777 vortices in an inversion capped planetary boundary layer, *Quarterly Journal of the Royal*
 778 *Meteorological Society*, 108, 801–823, doi:10.1002/qj.49710845805.
- 779 McGouldrick, K., and O. B. Toon (2008), Observable effects of convection and gravity
 780 waves on the Venus condensational cloud, *Plan. and Sp. Sci.*, 56, 1112–1131, doi:10.
 781 1016/j.pss.2008.02.010.
- 782 Moeng, C., J. Dudhia, J. Klemp, and P. Sullivan (2007), Examining Two-Way Grid Nest-
 783 ing for Large Eddy Simulation of the PBL Using the WRF Model, *Monthly Weather*
 784 *Review*, 135(6), 2295–2311.
- 785 Peralta, J., R. Hueso, A. Sánchez-Lavega, G. Piccioni, O. Lanciano, and P. Drossart
 786 (2008), Characterization of mesoscale gravity waves in the upper and lower clouds

- 787 of Venus from VEX-VIRTIS images, *J. of Geophys. Res. (Planets)*, *113*, E00B18, doi:
788 10.1029/2008JE003185.
- 789 Piccialli, A., D. V. Titov, A. Sánchez-Lavega, J. Peralta, O. Shalygina, W. J. Markiewicz,
790 and H. Svedhem (2014), High latitude gravity waves at the Venus cloud tops as ob-
791 served by the Venus Monitoring Camera on board Venus Express, *Icarus*, *227*, 94–111,
792 doi:10.1016/j.Icarus.2013.09.012.
- 793 Rossow, W. B., A. D. del Genio, S. S. Limaye, and L. D. Travis (1980), Cloud morphol-
794 ogy and motions from Pioneer Venus images, *Journal of Geophysical Research*, *85*,
795 8107–8128, doi:10.1029/JA085iA13p08107.
- 796 Sánchez-Lavega, A., S. Lebonnois, T. Imamura, P. Read, and D. Luz (2017), The At-
797 mospheric Dynamics of Venus, *Space Science Review*, *212*, 1541–1616, doi:10.1007/
798 s11214-017-0389-x.
- 799 Schubert, G., C. Covey, A. del Genio, L. S. Elson, G. Keating, A. Seiff, R. E. Young,
800 J. Apt, C. C. Counselman, A. J. Kliore, S. S. Limaye, H. E. Revercomb, L. A. Sro-
801 movsky, V. E. Suomi, F. Taylor, R. Woo, and U. von Zahn (1980), Structure and cir-
802 culation of the Venus atmosphere, *Journal of Geophysical Research*, *85*, 8007–8025,
803 doi:10.1029/JA085iA13p08007.
- 804 Seiff, A., D. B. Kirk, R. E. Young, R. C. Blanchard, J. T. Findlay, G. M. Kelly, and S. C.
805 Sommer (1980), Measurements of thermal structure and thermal contrasts in the at-
806 mosphere of Venus and related dynamical observations - Results from the four Pi-
807 oneer Venus probes, *Journal of Geophysical Research*, *85*, 7903–7933, doi:10.1029/
808 JA085iA13p07903.
- 809 Skamarock, W. C., and J. B. Klemp (2008), A time-split nonhydrostatic atmospheric
810 model for weather research and forecasting applications, *Journal of Computational*
811 *Physics*, *227*, 3465–3485.
- 812 Spiga, A., F. Forget, S. R. Lewis, and D. P. Hinson (2010), Structure and dynamics of the
813 convective boundary layer on mars as inferred from large-eddy simulations and remote-
814 sensing measurements, *Quarterly Journal of the Royal Meteorological Society*, *136*, 414–
815 428, doi:10.1002/qj.563.
- 816 Spiga, A., E. Barth, Z. Gu, F. Hoffmann, J. Ito, B. Jemmett-Smith, M. Klose,
817 S. Nishizawa, S. Raasch, S. Rafkin, T. Takemi, D. Tyler, and W. Wei (2016), Large-
818 Eddy Simulations of Dust Devils and Convective Vortices, *Space Science Reviews*, *203*,
819 245–275, doi:10.1007/s11214-016-0284-x.
- 820 Sullivan, P. P., and E. G. Patton (2011), The Effect of Mesh Resolution on Convective
821 Boundary Layer Statistics and Structures Generated by Large-Eddy Simulation, *Journal*
822 *of Atmospheric Sciences*, *68*, 2395–2415, doi:10.1175/JAS-D-10-05010.1.
- 823 Tellmann, S., B. Häusler, M. Paetzold, M. K. Bird, G. L. Tyler, T. Andert, and S. Remus
824 (2009), The Structure of the Venus Neutral Atmosphere as seen by the Radio Science
825 Experiment VeRa on Venus Express, *J. of Geophys. Res. (Planets)*, *114*, E00B36, doi:
826 10.1029/2008JE003204.
- 827 Tellmann, S., B. Häusler, D. P. Hinson, G. L. Tyler, T. P. Andert, M. K. Bird, T. Ima-
828 mura, M. Pätzold, and S. Remus (2012), Small-scale temperature fluctuations seen by
829 the VeRa Radio Science Experiment on Venus Express, *Icarus*, *221*, 471–480, doi:
830 10.1016/j.Icarus.2012.08.023.
- 831 Titov, D. V., W. J. Markiewicz, N. I. Ignatiev, L. Song, S. S. Limaye, A. Sánchez-Lavega,
832 J. Hesemann, M. Almeida, T. Roatsch, K.-D. Matz, F. Scholten, D. Crisp, L. W. Espos-
833 ito, S. F. Hviid, R. Jaumann, H. U. Keller, and R. Moissl (2012), Morphology of the
834 cloud tops as observed by the Venus Express Monitoring Camera, *Icarus*, *217*, 682–
835 701, doi:10.1016/j.icarus.2011.06.020.
- 836 Torrence, C., and G. P. Compo (1998), A practical guide to wavelet analysis, *Bulletin of*
837 *the American Meteorological Society*, *79*, 61–78.
- 838 Yamamoto, M. (2011), Microscale simulations of Venus convective adjustment and mixing
839 near the surface: Thermal and material transport processes, *Icarus*, *211*, 993–1006, doi:
840 10.1016/j.icarus.2010.11.019.

841
842

Yamamoto, M. (2014), Idealized numerical experiments on microscale eddies in the Ven-
sian cloud layer, *Earth, Planets, and Space*, *66*, 27, doi:10.1186/1880-5981-66-27.

Accepted Article

caption figure.

Accepted Article

FIG. 1 – Top : Vertical profile of the large-scale dynamical heating rate (10^{-4} K s^{-1}) between 45 and 57 km and from 57 to 75 km. Bottom : Vertical wind of the LMD Venus GCM in (Pa s^{-1}) at night (left) and noon (right) between 42 and 63 km. Positive value of vertical means downward wind and positive value means upward wind. The black lines represent the convective activity vertical extension.

FIG. 2 – The forcing in the Venus cloud region : solar, infrared (IR), large-scale dynamical and the total heating rates (K/s) in the equatorial condition at noon.

FIG. 3 – The Venus cloud mixing layer : domain averaged potential temperature (K) (left) and static stability (K/km) (right) between 42 and 65 km in the equatorial condition at noon.

FIG. 4 – Snapshots of the cloud convective vertical motions : vertical cross-section at $y = 20 \text{ km}$ between 42 and 65 km of altitude (left) and horizontal cross-section at 51 km of the vertical wind (m s^{-1}) (right) at the Equator at noon.

FIG. 5 – Domain averaged vertical profile of the turbulent heat flux (W m^{-2}) of the Venus cloud convective layer for Equatorial condition at noon.

FIG. 6 – Snapshots of the induced gravity waves : vertical cross-section at $y = 20 \text{ km}$ of the temperature perturbation (K) between 42 and 65 km (left) and horizontal cross-section at 57 km of the vertical wind perturbation (m s^{-1}) (right), at the Equator at noon.

FIG. 7 – Comparison of the vertical profile of the domain averaged static stability (K/km) for equatorial condition at noon and midnight between 42 and 63 km.

FIG. 8 – Comparison of the induced gravity waves : temperature perturbation (K) at the Equator for noon (left) and midnight (right) between 42 and 63 km.

FIG. 9 – Comparison of the vertical profile of the domain averaged static stability (K/km) for the Equator, 55° and 75° of latitude at noon (left) and midnight (right).

FIG. 10 – Vertical profile of the input zonal and meridional winds at noon (left) and midnight (right) for the Equator, 55° and 75° of latitude.

FIG. 11 – Comparison of the vertical profile of the domain averaged static stability (K/km) at cloud top between the presence of a wind shear and no wind shear for equatorial condition at midnight (left) and noon (right).

FIG. 12 – Impact of the wind shear : Comparison of two snapshots of the temperature perturbation (K) at the Equator at midnight without (left) and with (right) wind shear.

Accepted Article

FIG. 13 – Comparison of two snapshots of the vertical wind perturbation (m s^{-1}) at the Equator at midnight without (left) and with (right) wind shear.

FIG. 14 – Snapshots of the vertical wind perturbation (m s^{-1}) at 70 km at the Equator at midnight in presence of wind shear.

FIG. 15 – Domain averaged vertical momentum flux (mPa) above (left) and below (right) the convective layer at the equator.

FIG. 16 – Domain averaged vertical profile of potential temperature (K) (left) and static stability (K/km) (right) between 63 and 75 km at the equator at noon.

FIG. 17 – Snapshots of the convective vertical motions : vertical cross-section at $y=20$ km between 63 and 75 km (left) and horizontal cross-section at 51 km of the vertical wind (m s^{-1}) (right) for equatorial condition at noon.

FIG. 18 – Venus cloud top forcing : solar (SW), infrared (LW), dynamical (DYN) and total (DT) heating rates (K/s) between 63 and 75 km at the equator at noon.

FIG. 19 – Domain averaged vertical profile of the turbulent heat flux (W m^{-2}) of the Venus cloud top convection between 63 and 75 km for equatorial condition at noon.

FIG. 20 – Comparison of the domain averaged static stability vertical profile (K/km) for equatorial conditions at noon and at midnight between 63 and 75 km.

FIG. 21 – Comparison of the domain averaged static stability vertical profile (K/km) at noon (LT 12 h), for the Equator, 55° latitude and 75° latitude between 63 and 75 km.

Accepted Article

fig 1.

Accepted Article

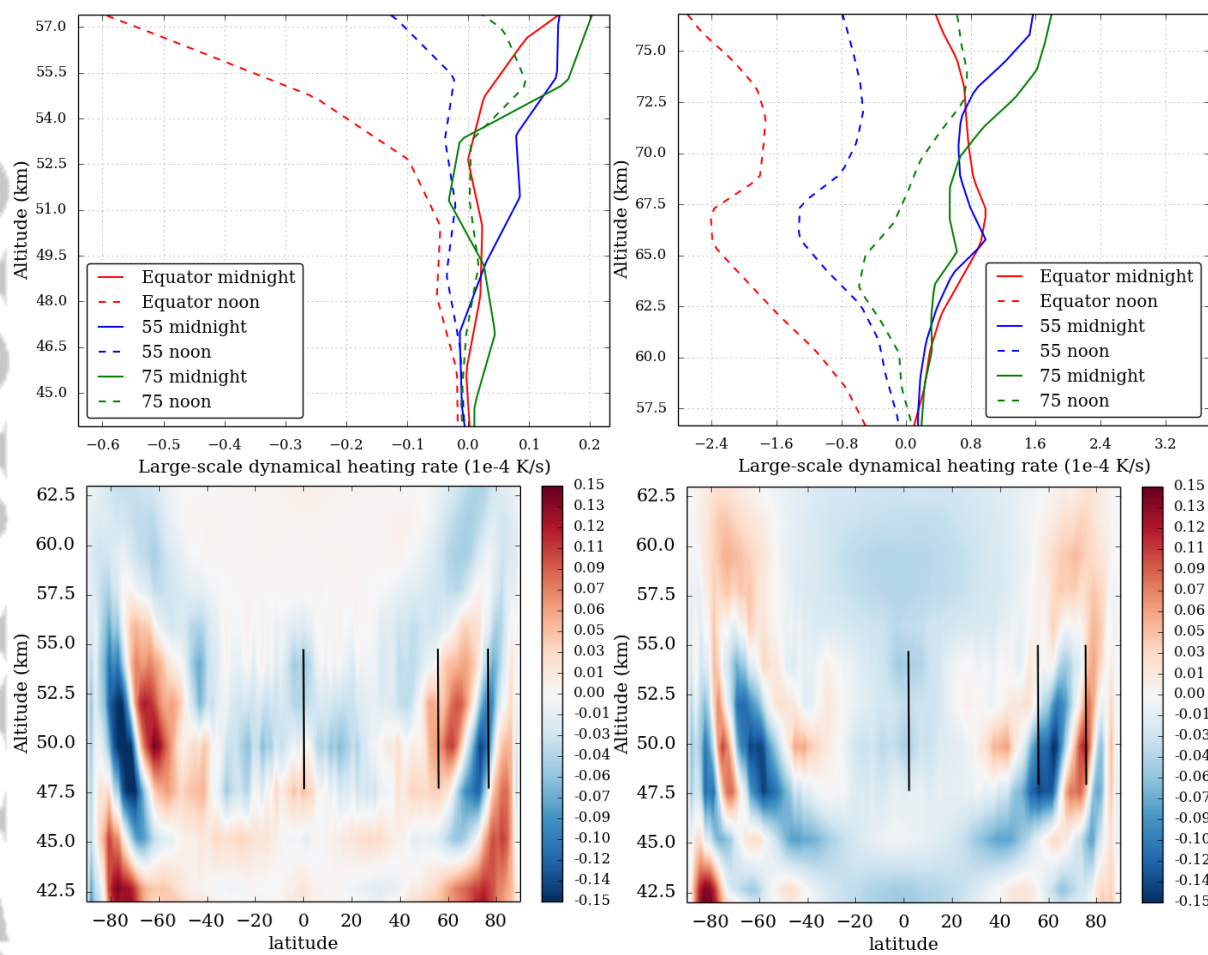


fig 2.

Accepted Article

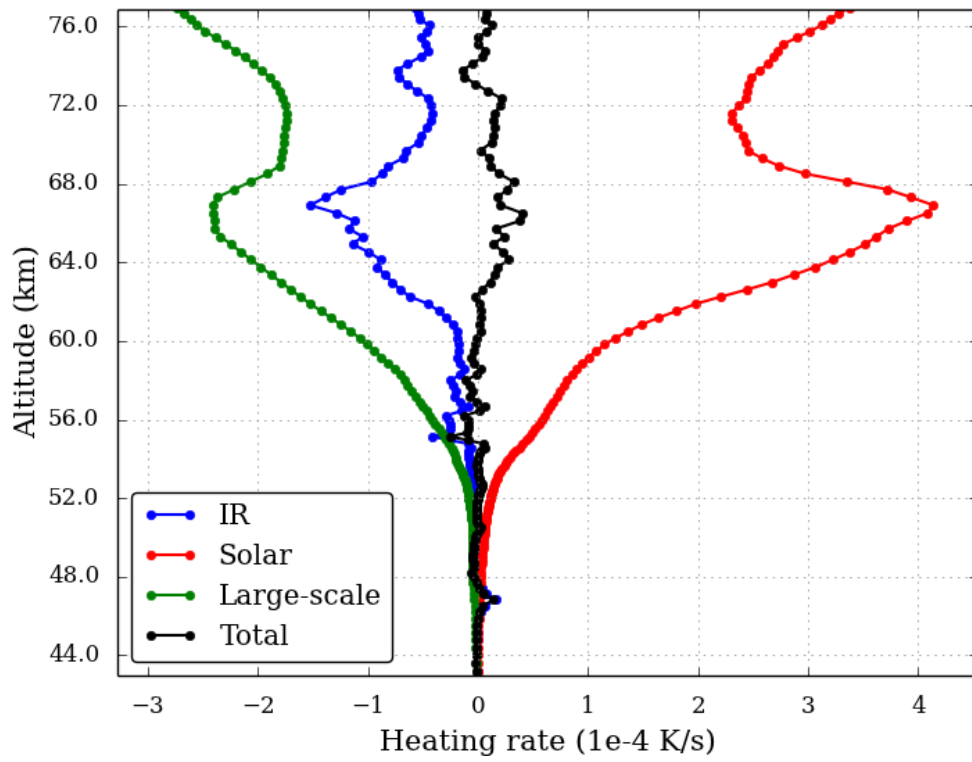


fig 3.

Accepted Article

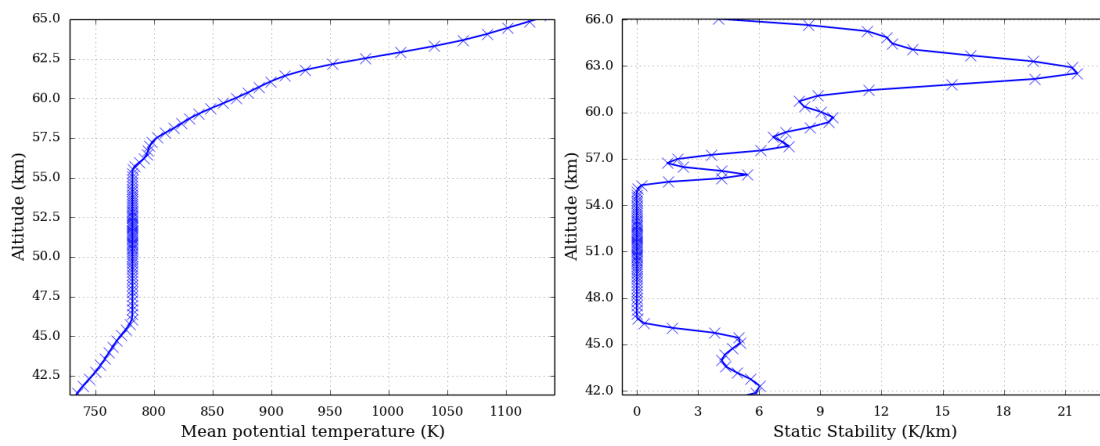


fig 4.

Accepted Article

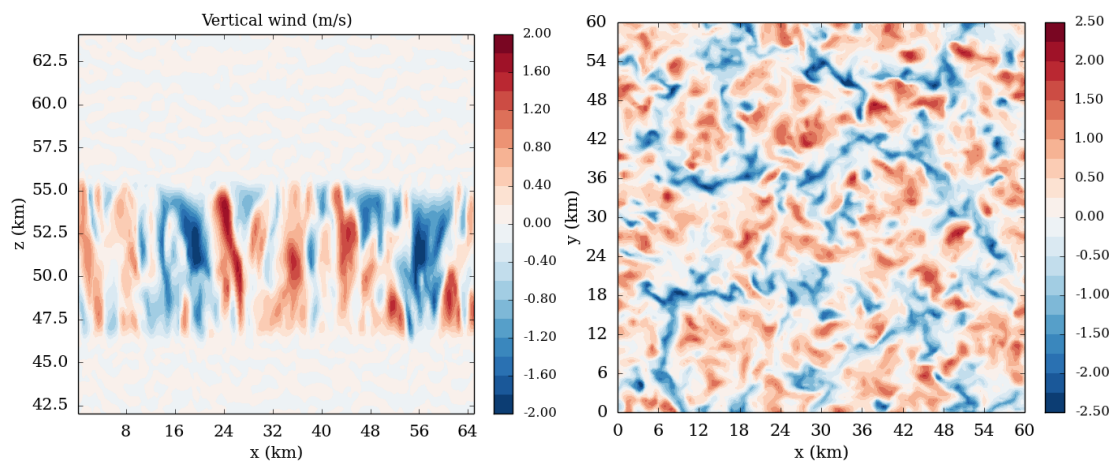


fig 5.

Accepted Article

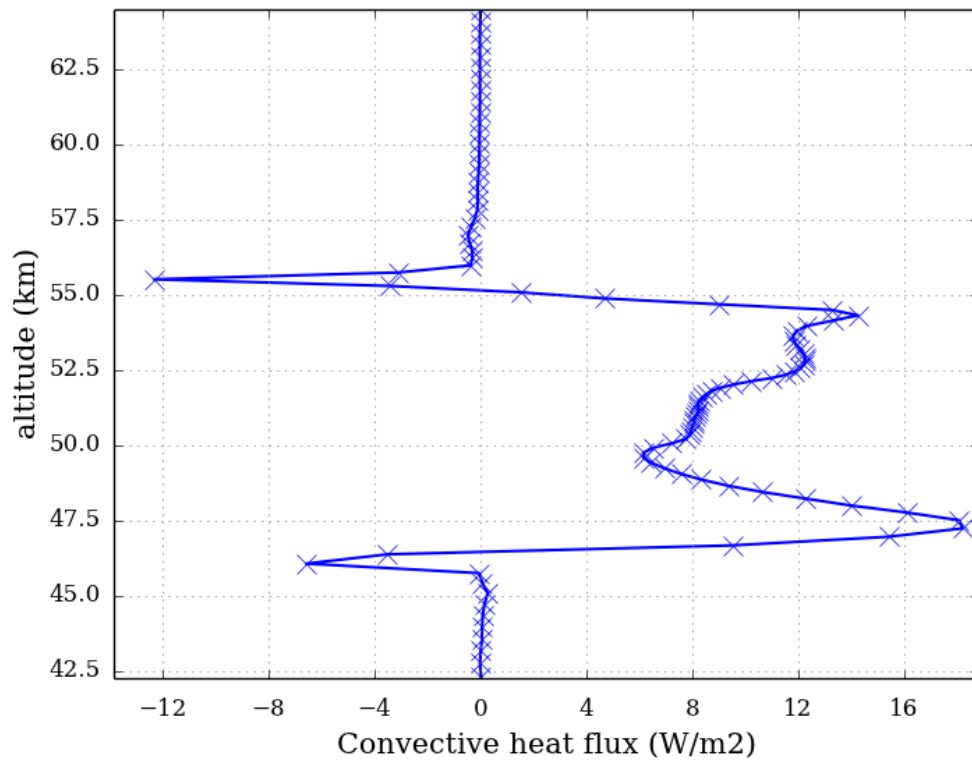


fig 6.

Accepted Article

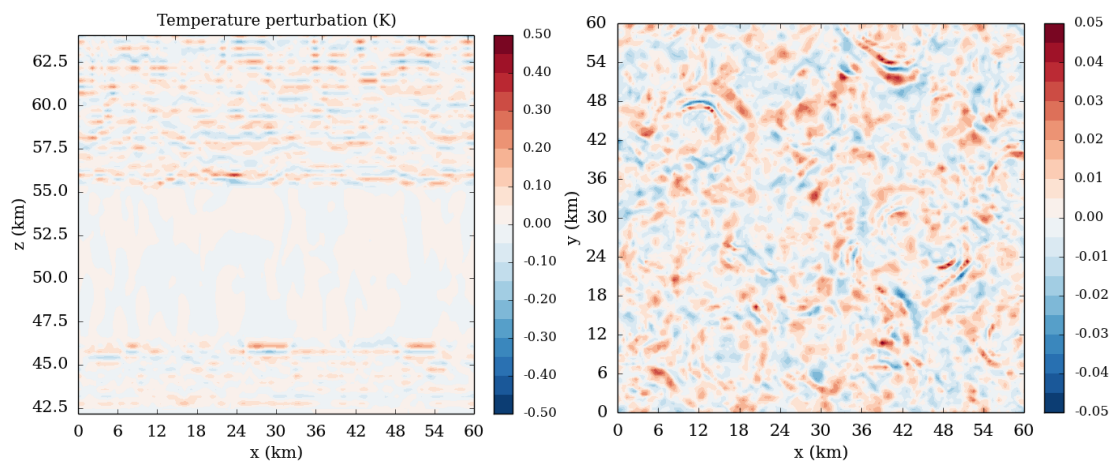


fig 7.

Accepted Article

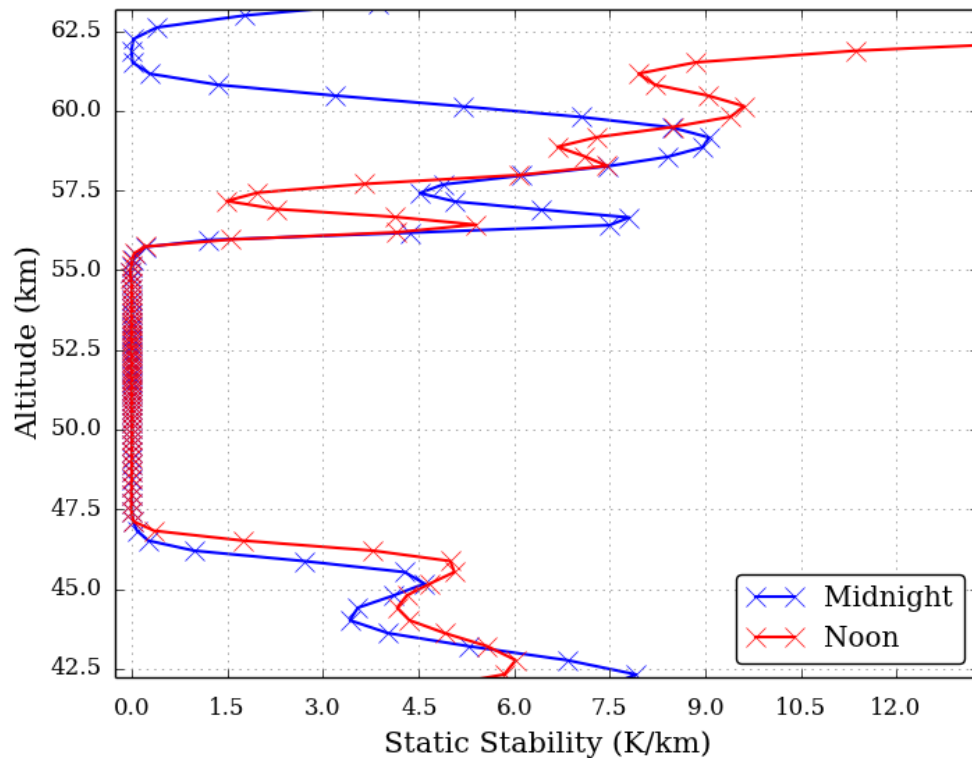


fig 8.

Accepted Article

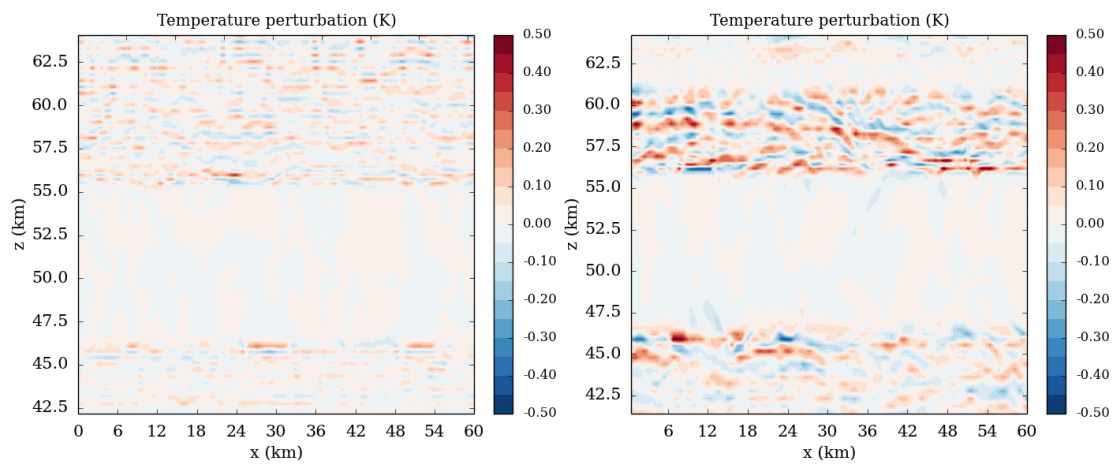


fig 9.

Accepted Article

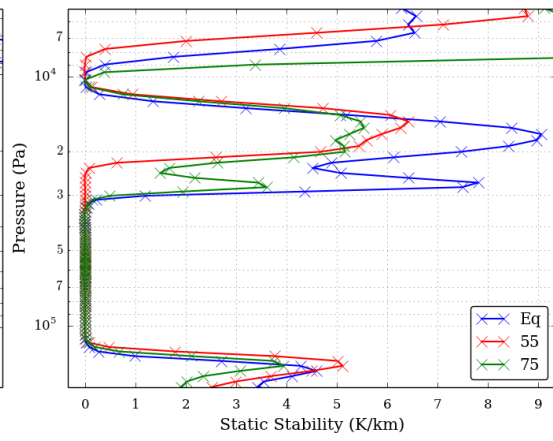
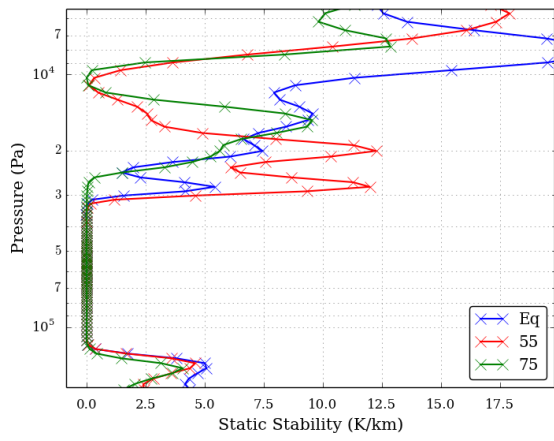


fig 10.

Accepted Article

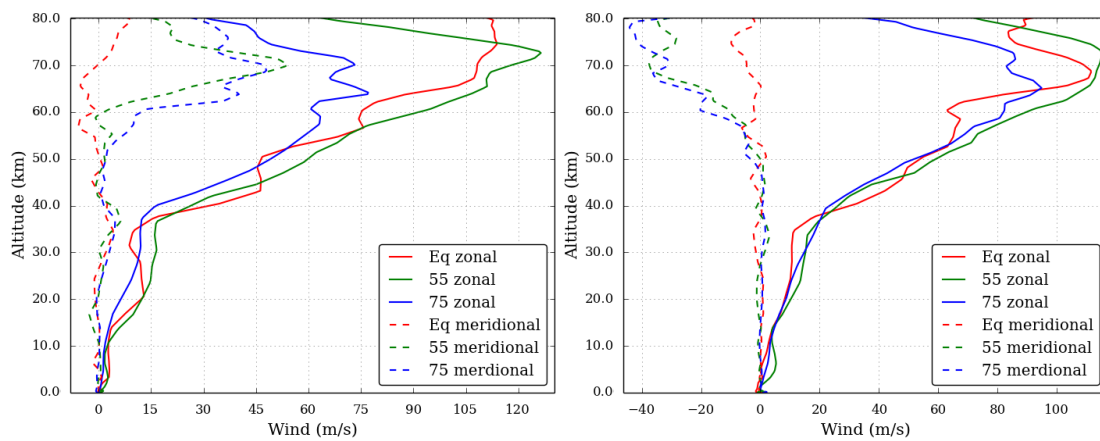
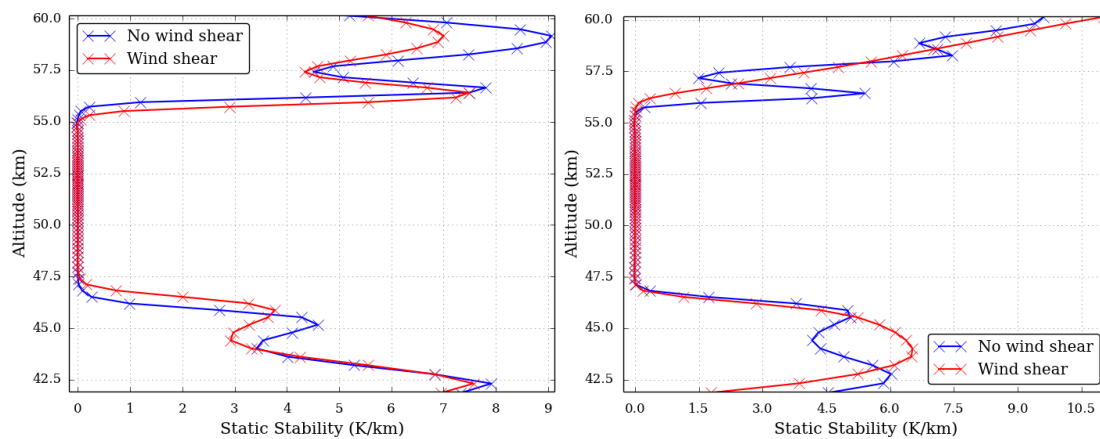
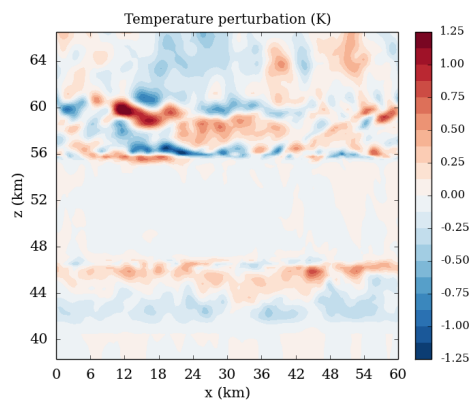
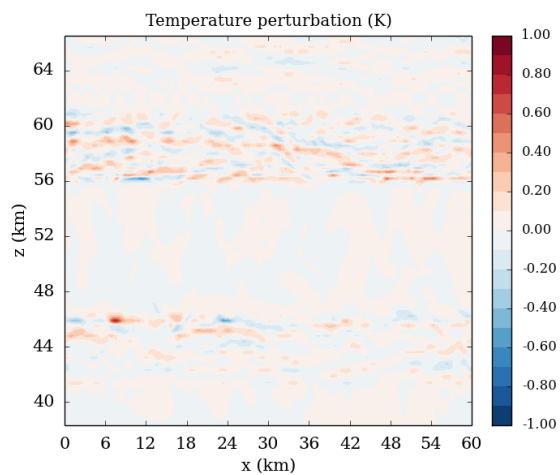


fig 11.

Accepted Article



Accepted Article



Accepted Article

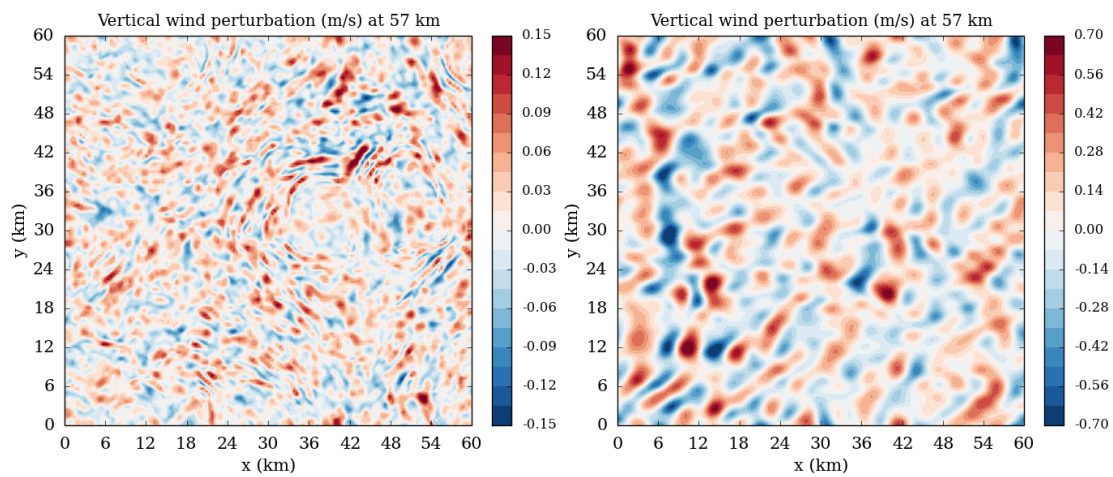
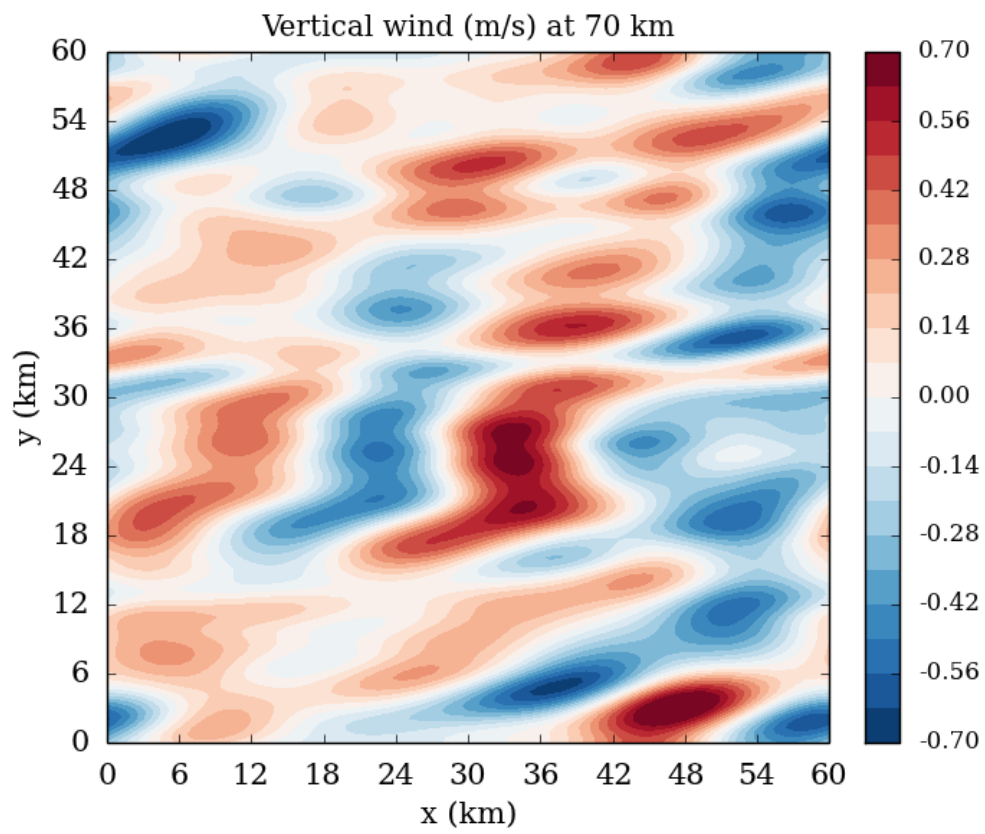


fig 14.

Accepted Article



Accepted Article

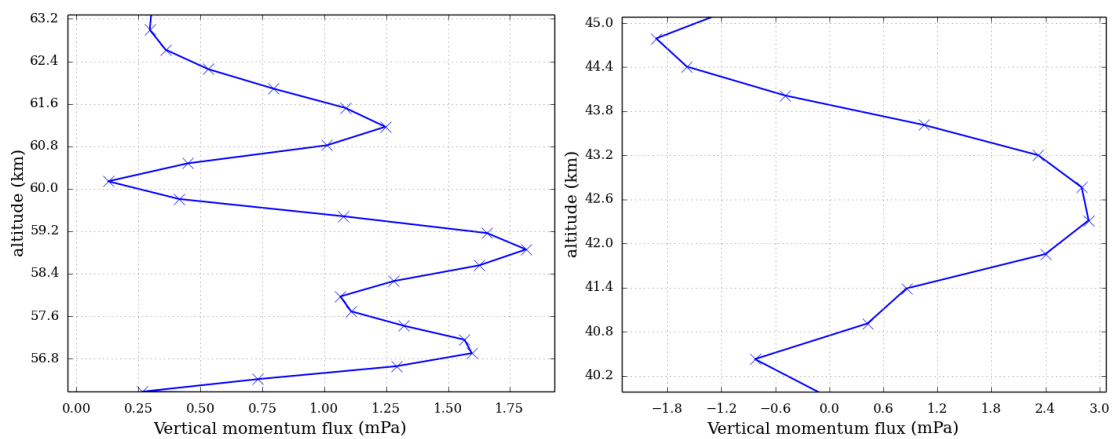


fig 16.

Accepted Article

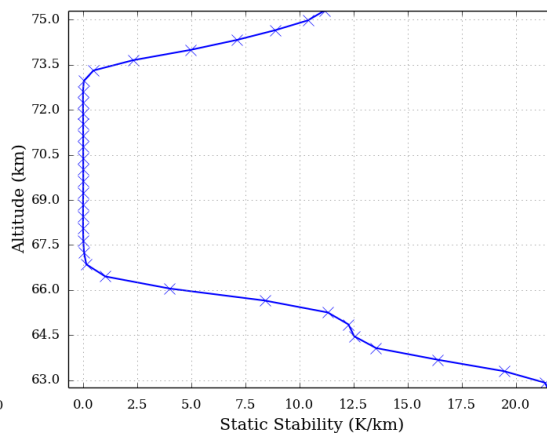
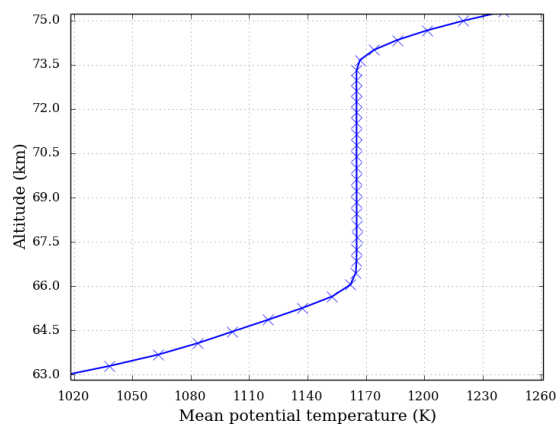
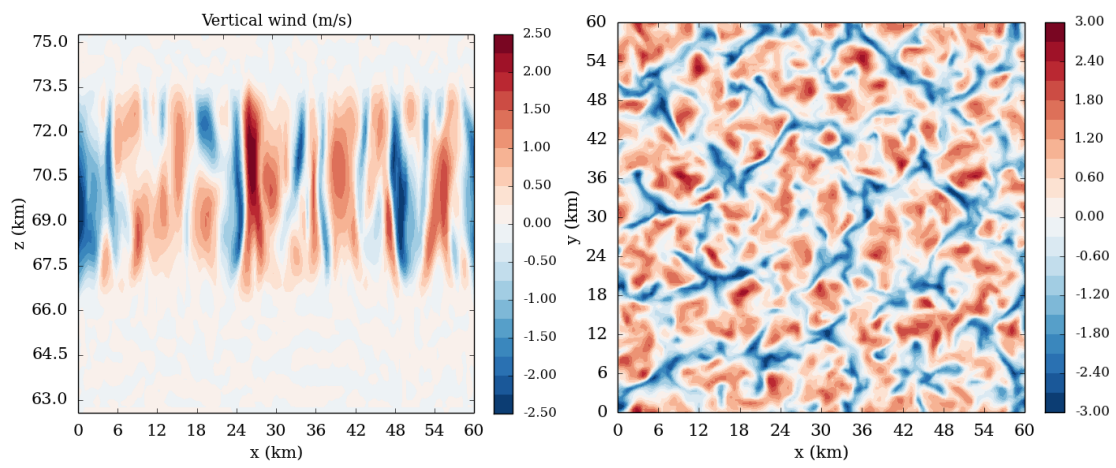
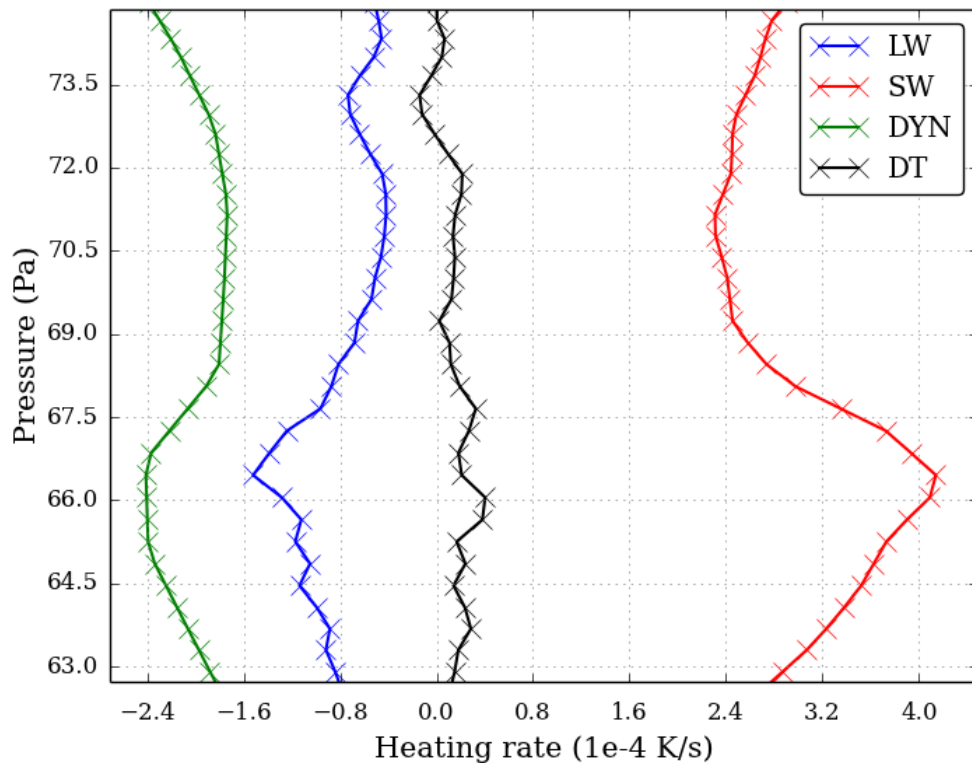


fig 17.

Accepted Article



Accepted Article



Accepted Article

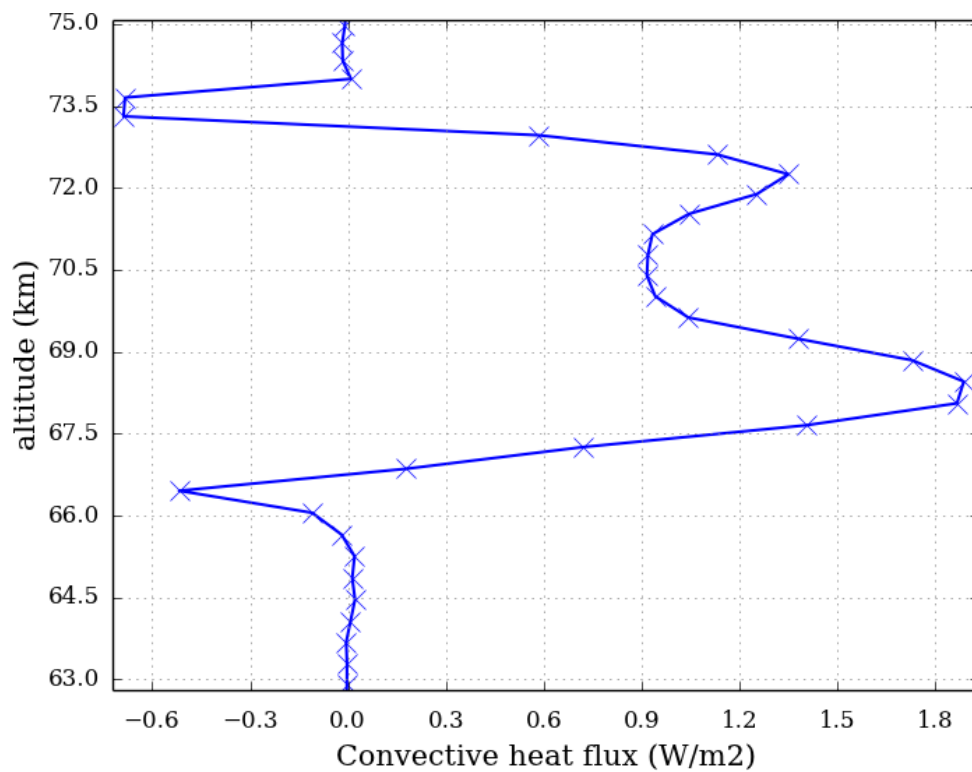


fig 20.

Accepted Article

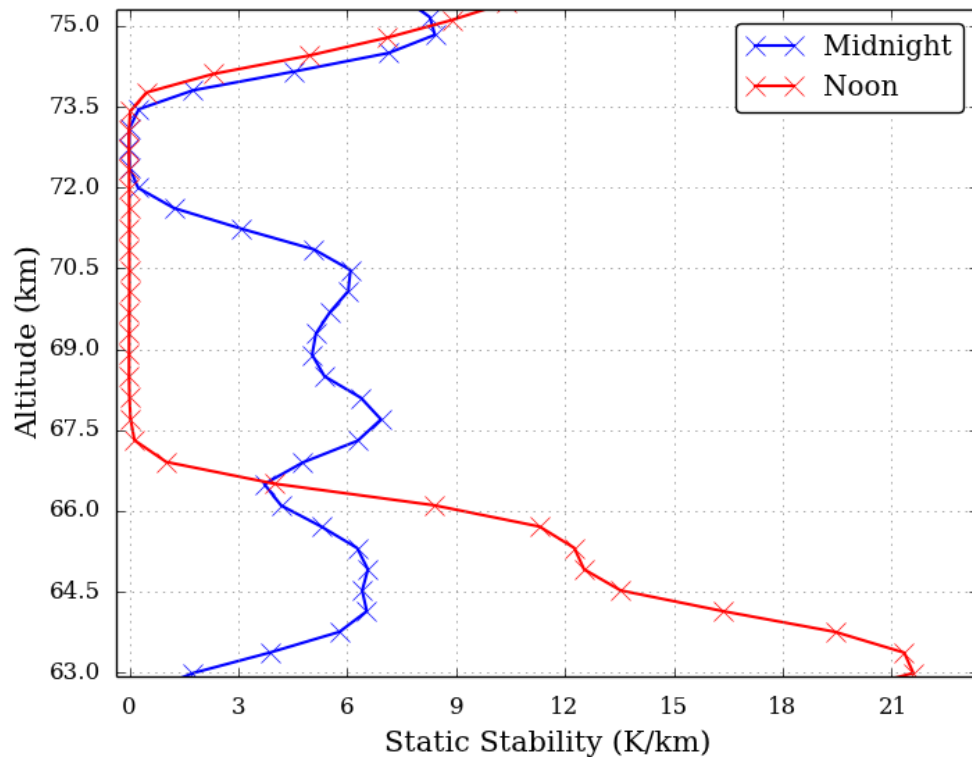


fig 21.

Accepted Article

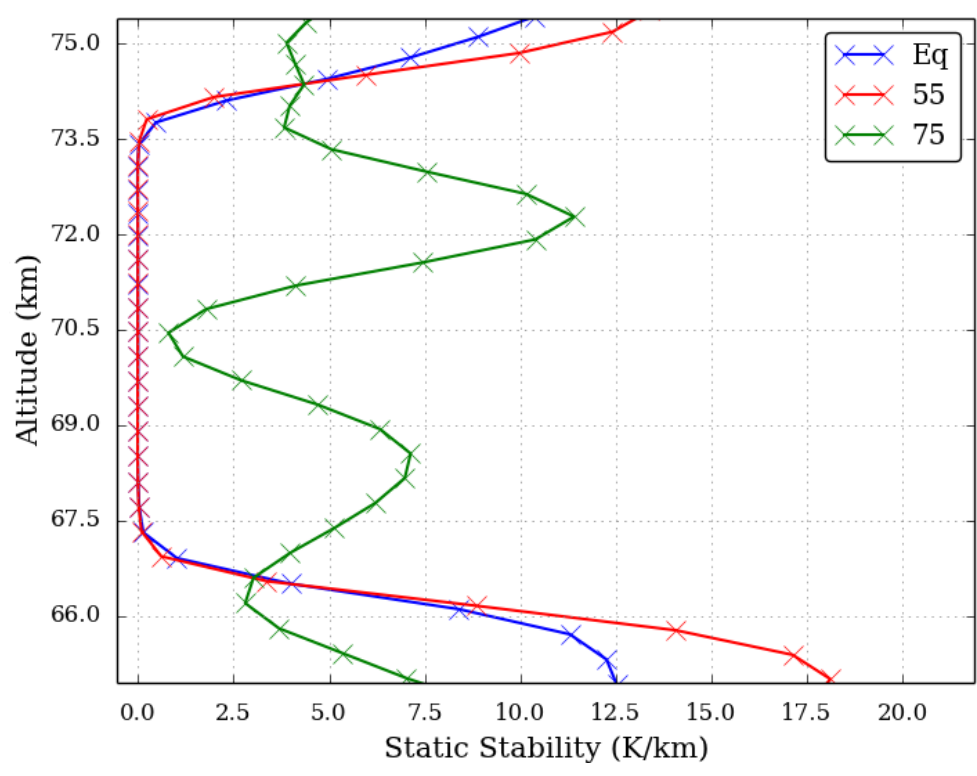


FIG. 1 – Top : Vertical profile of the large-scale dynamical heating rate (10^{-4} K s^{-1}) between 45 and 57 km and from 57 to 75 km. Bottom : Vertical wind of the LMD Venus GCM in (Pa s^{-1}) at night (left) and noon (right) between 42 and 63 km. Positive value of vertical means downward wind and positive value means upward wind. The black lines represent the convective activity vertical extension.

FIG. 2 – The forcing in the Venus cloud region : solar, infrared (IR), large-scale dynamical and the total heating rates (K/s) in the equatorial condition at noon.

FIG. 3 – The Venus cloud mixing layer : domain averaged potential temperature (K) (left) and static stability (K/km) (right) between 42 and 65 km in the equatorial condition at noon.

FIG. 4 – Snapshots of the cloud convective vertical motions : vertical cross-section at $y = 20 \text{ km}$ between 42 and 65 km of altitude (left) and horizontal cross-section at 51 km of the vertical wind (m s^{-1}) (right) at the Equator at noon.

FIG. 5 – Domain averaged vertical profile of the turbulent heat flux (W m^{-2}) of the Venus cloud convective layer for Equatorial condition at noon.

FIG. 6 – Snapshots of the induced gravity waves : vertical cross-section at $y = 20 \text{ km}$ of the temperature perturbation (K) between 42 and 65 km (left) and horizontal cross-section at 57 km of the vertical wind perturbation (m s^{-1}) (right), at the Equator at noon.

FIG. 7 – Comparison of the vertical profile of the domain averaged static stability (K/km) for equatorial condition at noon and midnight between 42 and 63 km.

FIG. 8 – Comparison of the induced gravity waves : temperature perturbation (K) at the Equator for noon (left) and midnight (right) between 42 and 63 km.

FIG. 9 – Comparison of the vertical profile of the domain averaged static stability (K/km) for the Equator, 55° and 75° of latitude at noon (left) and midnight (right).

FIG. 10 – Vertical profile of the input zonal and meridional winds at noon (left) and midnight (right) for the Equator, 55° and 75° of latitude.

FIG. 11 – Comparison of the vertical profile of the domain averaged static stability (K/km) at cloud top between the presence of a wind shear and no wind shear for equatorial condition at midnight (left) and noon (right).

FIG. 12 – Impact of the wind shear : Comparison of two snapshots of the temperature perturbation (K) at the Equator at midnight without (left) and with (right) wind shear.

FIG. 13 – Comparison of two snapshots of the vertical wind perturbation (m s^{-1}) at the Equator at midnight without (left) and with (right) wind shear.

FIG. 14 – Snapshots of the vertical wind perturbation (m s^{-1}) at 70 km at the Equator at midnight in presence of wind shear.

FIG. 15 – Domain averaged vertical momentum flux (mPa) above (left) and below (right) the convective layer at the equator.

FIG. 16 – Domain averaged vertical profile of potential temperature (K) (left) and static stability (K/km) (right) between 63 and 75 km at the equator at noon.

FIG. 17 – Snapshots of the convective vertical motions : vertical cross-section at $y=20$ km between 63 and 75 km (left) and horizontal cross-section at 51 km of the vertical wind (m s^{-1}) (right) for equatorial condition at noon.

FIG. 18 – Venus cloud top forcing : solar (SW), infrared (LW), dynamical (DYN) and total (DT) heating rates (K/s) between 63 and 75 km at the equator at noon.

FIG. 19 – Domain averaged vertical profile of the turbulent heat flux (W m^{-2}) of the Venus cloud top convection between 63 and 75 km for equatorial condition at noon.

FIG. 20 – Comparison of the domain averaged static stability vertical profile (K/km) for equatorial conditions at noon and at midnight between 63 and 75 km.

FIG. 21 – Comparison of the domain averaged static stability vertical profile (K/km) at noon (LT 12 h), for the Equator, 55° latitude and 75° latitude between 63 and 75 km.

Accepted Article

